International Journal of Solids and Structures 281 (2023) 112412

Contents lists available at ScienceDirect

International Journal of Solids and Structures

journal homepage: www.elsevier.com/locate/ijsolstr

# Bounding surface plasticity model modification for ratcheting of metals

Yannis F. Dafalias [a,b,c], Alexandros L. Petalas [d,*], Heidi Feigenbaum [e]

[a] Department of Civil and Environmental Engineering, University of California, Davis, USA
[b] Institute of Thermomechanics, Czech Academy of Sciences, Prague, Czech Republic
[c] School of Applied Mathematical and Physical Sciences, Department of Mechanics, National Technical University of Athens, Greece
[d] Department of Engineering, Durham University, UK
[e] Department of Mechanical Engineering, Northern Arizona University, Flagstaff, AZ 86011, USA

ARTICLE INFO

*Keywords:*
Plasticity
Constitutive modeling
Ratcheting of metals
Bounding surface
Kinematic hardening

ABSTRACT

The Bounding Surface (BS) plasticity model for metals is modified according to the proposition introduced in the works of Burlet and Cailletaud (1986) and Delobelle (1993) for the kinematic hardening of a classical Armstrong/Frederick (AF) model, called the BCD modification from the initials of the foregoing authors. The BCD modification was introduced in the relative kinematic hardening between Yield Surface (YS) and BS, unlike its introduction in the absolute and single kinematic hardening of YS for an AF model, hence, achieving two objectives: first, maintaining the inherent feature of BS for decoupling plastic modulus and direction of kinematic hardening, and, second, allowing a flexibility as to the relative kinematic hardening direction without altering the value of the plastic modulus, a property of BCD modification. In addition, the introduced BCD modification for the BS is significantly modified itself, by introducing a properly varying modification parameter instead of the fixed one used in the original works. This simple feature of the novel BCD modification provides a dramatically improved capability to simulate multiaxial ratcheting (MR), because it affects directly the changing flow rule direction, due to the relative kinematic hardening, during complex multiaxial loading, without sacrificing accurate simulations under uniaxial ratcheting (UR) since the plastic modulus is not affected. An additional significant contribution to successful UR simulations is provided by the free-to-choose kinematic hardening of the BS, since the BCD modification is applied only to the relative kinematic hardening between BS and YS. The new model, named SANIMETAL-BCD, is shown to yield superior or equal simulations of UR and very complex MR experimental data for three Carbon Steel specimens, in comparison with other models, within a much simpler constitutive framework. Shortcomings and future necessary improvements are discussed in details.

## 1. Introduction

Ratcheting is a term referring to the accumulation of plastic strain under the imposition of stress or strain (in multiaxial cases) cyclic loading; in the uniaxial case, the cyclic stress has a non-zero mean value. It is in fact a more difficult response to model than "symmetric" cyclic loading where the cyclic stress has a zero-mean value, but it is also more important in practice because this is the expected way metal components are loaded in all kinds of structures, e.g., piping components in chemical or nuclear plants, beam and column elements as well as their connections in metal frames, etc. Ratcheting is distinguished into Uniaxial and Multiaxial Ratcheting, henceforth abbreviated as UR and MR, respectively.

As per its name, UR is characterized by one non-zero stress component cycling over its own non-zero mean value and, therefore, causing accumulation of the corresponding uniaxial plastic strain component, while because of incompressibility additional predefined strain components appear. In stress-controlled MR, there is at least one cyclically varying stress component of zero or non-zero mean value, imposed on one (at least) pre-existing different non-zero stress component, that usually remains fixed. In strain-controlled MR, a total strain component is cycled instead of the stress. In stress-controlled MR there are more than one plastic strain components that accumulate along the directions of non-zero stress components, notwithstanding the additional strain components needed for the satisfaction of plastic incompressibility for metals. For strain-controlled MR, the cycled strain has fixed values, but there is at least one other strain component that accumulates, while the stress corresponding to the cycled strain component increases (hardening) or decreases (softening). One very common and useful example of MR occurs when a pipe is under fixed or varying internal pressure and is cyclically loaded under axial stress or strain control. Both

* Corresponding author.
*E-mail addresses:* jfdafalias@ucdavis.edu (Y.F. Dafalias), alexandros.petalas@durham.ac.uk (A.L. Petalas), Heidi.Feigenbaum@nau.edu (H. Feigenbaum).

https://doi.org/10.1016/j.ijsolstr.2023.112412
Received 16 January 2023; Received in revised form 6 June 2023; Accepted 5 July 2023
Available online 18 July 2023

axial and circumferential strain components accumulate in a stress-controlled experiment, while if one strain component is prescribed in a strain-controlled experiment, it is the other strain component that accumulates.

The research objective of this paper is to address the constitutive modeling of UR and MR of metals, by proper modifications of the plasticity constitutive model introduced in the mid-seventies by Dafalias and Popov (1974, 1975, 1976) and updated by Mahan et al. (2011), that uses the coupling interaction of two surfaces, the Yield Surface (YS) and the Bounding Surface (BS) which encloses the YS. A similar theory was simultaneously introduced by Krieg (1975), but the format was very different and not applicable to the demands for MR simulations, such as the necessity to have the BS obeying Isotropic Hardening (IH) and special kind of Kinematic Hardening (KH) not existing in the Krieg's formulation.

UR and MR have been the objectives of a multitude of research efforts and publications, yet simulation of many available data has not been entirely satisfactory; in fact, it was rather unsuccessful in several cases, particularly for MR, and often required the introduction of complicated additional constitutive features. One can say that the problem of MR simulations, despite its very long history that counts several decades, is not resolved at a satisfactory level from the perspective of both accurate predictions and relatively simple constitutive modeling.

There are two main categories of constitutive models used for metal ratcheting, both based on the concept of back-stress and associated KH, that can also include, if necessary, IH. The first kind is based on the seminal work by Armstrong and Frederick (1966) who proposed the so-called evanescent memory model, named AF model here for abbreviation, that extended the linear KH models of Ishlinskii (1954) and Prager (1956) to a non-linear KH format for the back stress. Due to several inherent problems of this model, mainly for partial unloading/reloading as explained later by Dafalias (1984), Chaboche et al. (1979) have introduced a Multicomponent Armstrong/Frederick model, named MAF for abbreviation, that additively combines several AF back-stress components to get the total back stress, providing the tools for successful cyclic loading simulations. It was used towards MR with relative success, often requiring modification of the AF basic KH rule by several authors who introduced additional constitutive features such as non-hardening regions or memory surfaces in strain or stress space, etc., a complete list of which is beyond the scope and objectives of this paper. MAF-based models are by far the most used and investigated models in cyclic plasticity for metals today. It is worth mentioning that Marquis (1979) has shown that any classical AF model implies the existence of a fixed limit surface in stress space, with which the back stress converges without ever crossing it, such limit surface acting in essence as a fixed BS for the back-stress rather than the stress.

The second category of constitutive models is based on BS plasticity, mentioned earlier. The original two-surface BS version by Dafalias and Popov (1974, 1975, 1976) and Krieg (1975) were motivated by the multi-surface model of Mróz (1967) but were developed on an entirely different platform. The Mróz (1967) model, while very successful for certain kinds of cyclic loading simulations, has not been used for UR and MR simulations because of an inherent early stabilization of the strain accumulation due to its basic conception and formulation that yields closed loops in uniaxial cyclic loading. The successful application of the BS model to random cyclic loading in the uniaxial case and some multiaxial loading paths was established earlier than that of MAF models. However, its application to MR was delayed because, unlike the inventors and followers of MAF models who pursued further the development of their model, the inventors of BS have switched their attention to its use for soil plasticity constitutive modeling under triaxial and multiaxial cyclic loading, where now BS-based models hold a dominant position under the code names SANICLAY and SANISAND models.

It took more than 15 years after the introduction of BS in 1975, for the research teams of Kyriakides and Hassan (e.g. Hassan and Kyriakides, 1992, 1994a,b; Hassan et al., 1992; Corona et al., 1996; Bari and Hassan, 2001) to discover the importance of two special constitutive features that characterize any BS model, in relation to UR and MR simulations of metals. First, the freedom to choose any kind of KH and IH for the BS, which allows one to obtain a bounding plastic modulus that affects the actual plastic modulus by the stress distance dependence of the two moduli within the general BS theory (Dafalias, 1986). Second, the ability to define the direction of the KH of the YS independently from the definition of the plastic modulus as described above, which is an inherent property for any BS model. This is often called the "decoupling" or "uncoupling" of these two quantities (e.g., Hassan and Kyriakides, 1992; Bari and Hassan, 2001), but note that the quantities are still connected to satisfy the consistency condition of plasticity. These two features provide great modeling flexibility because one could address the magnitude of plastic strain increment and simulate successfully UR based on the value of plastic modulus, and independently address the direction of KH for the YS that affects the evolution of the flow rule direction, and consequently the relative to each other norms of various plastic strain rate components, a key for successful simulation of MR, without altering the value of plastic modulus due to its independence from the choice of KH for the YS.

These two constitutive features are lacking from all MAF models because the AF KH rule and its variations define simultaneously plastic modulus and KH direction in a coupled and inflexible way. The research team of Kyriakides used the flexibility offered by BS with a small twist, namely, choosing the direction of an AF KH rule for the YS and independently the bounding plastic modulus resulting from a particular KH for the BS introduced in the dissertation of Sayed-Ranjbari (1986) and more recently updated in Mahan et al. (2011), where it was named the Dafalias/Ranjbari (DR) KH. In other words they ended up not using the direction of the DR KH for the BS but only the value of the ensuing bounding plastic modulus, while the direction of KH for the BS was defined by its interaction with the chosen AF KH of the YS. This approach brought the simulation of UR and MR, mainly for Carbon Steel (CS) specimens, in a better state than that of existing MAF models, by simpler constitutive means.

Yet, the final simulation of MR was not very successful in several cases, either by using MAF in all its variants or BS in the format used by the aforementioned researchers. Therefore, as mentioned earlier, the main objective of the present paper aims at modifying the BS model in such a way as to achieve simulations of equal or better accuracy for both UR and MR than those obtained by either MAF or previous BS models and achieve this while maintaining the greatest possible simplicity of the formulation. The proposed BS model modification in the sequel is motivated by two modifications introduced quite earlier for Prager and AF KH models. The first was a radial loading modification of a Prager linear KH model to a non-linear one, introduced by Burlet and Cailletaud (1986). The second, and more important modification for the current development, was a KH resulting from combining the aforementioned Prager non-linear and the usual evanescence memory KH of an AF model, introduced by Delobelle (1993). For abbreviation, it will be named the BCD modification from the initials of the aforementioned authors, without repeating the relevant references above. The nice feature of the BCD modification for an AF KH model was that one could modify the direction of KH by means of a new parameter $\delta$, called here the BCD modification parameter, that did not affect the value of the plastic modulus once the consistency condition was imposed, as if $\delta$ was never introduced. This provided AF with a flexibility similar to that of BS models (but not quite the same) on the choice of various KH directions with same plastic modulus by varying the value of $\delta$, which could be a function of other quantities such as max and mean values of back stress as well as of a non-radiality parameter (Delobelle, 1993; Delobelle et al., 1995). In fact, the BCD modification was applied to each component of a MAF model by Bari and Hassan (2001), with a fixed but different for each component BCD modification parameter, which improved MR simulations in many but not all cases.

Dafalias and Feigenbaum (2011) have proven analytically a serious theoretical shortcoming of the BCD modification, namely the choice of $\delta < 0.5$ can cause under specific loading conditions a crossing of the previously mentioned AF implied limit surface (Marquis, 1979), by the corresponding back-stress, i.e., the center of the YS, that can induce unwanted negative plastic modulus value and softening. Many of the successful simulations of prior works using MAF models with the BCD modification were employing such values of $\delta < 0.5$, but the unwanted negative plastic modulus value did not appear simply because the corresponding necessary loading conditions were not encountered in these particular simulations. Subsequently, Dafalias and Feigenbaum (2011) used in lieu of a fixed BCD modification parameter $\delta$, the variable ratio $r_i$ of the norm of the YS center, i.e., the norm of the $i$th back stress component, to the size of the $i$th AF limit surface, in their own MAF model with BCD modification that also included a multiplicative version of AF (Dafalias et al., 2008), avoiding the foregoing shortcoming because $r_i = 1$ on the $i$th limit surface. These changes improved further MR but still with unsatisfactory deviations for several data.

It seems, therefore, that MAF models, even with the BCD modification in various variants, are not capable of addressing satisfactorily MR in all cases, and often need to use additional constitutive features that complicate the formulation. We believe the cause is still the lack of complete decoupling between the KH direction of the YS and the plastic modulus in MAF models, as well as their lack of freedom to choose specific KH for the BS with the aforementioned beneficiary effects on plastic modulus, features that only BS models can offer together. Hence, it was decided to use two novel constitutive ingredients within the general BS theory. First, the introduction of a BCD modification into the relative KH of the YS with respect to the KH of the BS, such BS acting on the back stress of the YS rather than the stress on YS (as done by the limit surface in any AF model, clearly explained in Marquis, 1979). Second, the use of a variable quantity for the BCD modification parameter, that remains greater than 0.5 when the YS back stress reaches the BS to avoid the aforementioned shortcoming. Such quantity is motivated by, but also is quite different from, the one used in Dafalias and Feigenbaum (2011) for AF models, and its exact definition will be presented in the relevant part of this work. In addition, the BS will obey the DR KH, yielding not only the ensuing bounding plastic modulus used in Kyriakides and collaborators' works but also the implied DR KH direction. This relatively simple and straightforward approach produced successful simulations for both UR and MR that are equal or better than the existing ones by other models of greater complexity. Such simulations will be reported in the sequel, following first a rigorous analytical formulation as well as a guideline for calibration.

All tensors will be represented in direct notation by boldface symbols, a dot superposed on a quantity will imply its rate, while the symbol ":" between two tensors will imply the summation operation over the adjacent two pairs of indices in reverse order, which become the trace of the product of the two tensors if they are of the same rank. It is also convenient to list below the meaning of the main abbreviations used so far, to be repeated very often in this work:

MR: Multiaxial Ratcheting
UR: Uniaxial Ratcheting
BS: Bounding Surface
YS: Yield Surface
KH: Kinematic Hardening
IH: Isotropic Hardening
AF: Armstrong/Frederick
MAF: Multicomponent Armstrong/Frederick
DR: Dafalias/Ranjbari
BCD: Burlet/Cailletaud/Delobelle
CS: Carbon Steel

## 2. Classical plasticity formulation with IH and BCD modification of AF KH

A general classical plasticity formulation with Mises's type YS obeying IH and KH, consists of the following equations:

$$f = \frac{3}{2}(\boldsymbol{s}-\boldsymbol{\alpha}) : (\boldsymbol{s}-\boldsymbol{\alpha}) - k^2 = 0 \tag{1}$$

$$\dot{k} = \langle\lambda\rangle\bar{k} \tag{2}$$

$$\dot{\boldsymbol{\alpha}} = \langle\lambda\rangle\bar{\boldsymbol{\alpha}} \tag{3}$$

$$\dot{\boldsymbol{\varepsilon}}^p = \langle\lambda\rangle\boldsymbol{n} \tag{4}$$

with $f = 0$ the analytical expression of YS, $\boldsymbol{s}$ the deviatoric stress tensor, $\boldsymbol{\alpha}$ the deviatoric back stress tensor, $k$ the "size" of the YS, $\dot{\boldsymbol{\varepsilon}}^p$ the plastic strain rate tensor, $\bar{k}$ and $\bar{\boldsymbol{\alpha}}$ appropriate scalar and tensor valued functions, respectively, of the state variables $\boldsymbol{s}$ (external) and $\boldsymbol{\alpha}$, $k$ (internal), $\boldsymbol{n} = \sqrt{3/2}(\boldsymbol{s}-\boldsymbol{\alpha})/k$ the unit-norm tensor normal to the YS such that $\boldsymbol{n}$: $\boldsymbol{n} = 1$, $\lambda$ the loading index (or plastic multiplier), $< >$ the Macauley brackets such that $< A > = A$ when $A > 0$ and $< A > = 0$ when $A \leq 0$. Since $\boldsymbol{n}$ is a deviatoric tensor it follows that $\dot{\boldsymbol{\varepsilon}}^p = \dot{\boldsymbol{e}}^p$, with $\dot{\boldsymbol{e}}^p$ the deviatoric plastic strain rate. Clearly the plastic volumetric strain rate $tr\dot{\boldsymbol{\varepsilon}}^p = 0$, where $\varepsilon tr \varepsilon$ signifies the trace of a tensor.

The loading index $\lambda$ is obtained from the consistency condition $\dot{f} = 0$, which in conjunction with Eqs. (2) and (3), the preferred unit normal formulation, i.e., use of $\boldsymbol{n}$ instead of $\partial f/\partial\boldsymbol{\sigma}$ for the definition of $\lambda$ and the relations $\partial f/\partial k = -2k$ and $\partial f/\partial\boldsymbol{\sigma} = 3(\boldsymbol{s}-\boldsymbol{\alpha}) = -\partial f/\partial\boldsymbol{\alpha} = |\partial f/\partial\boldsymbol{\sigma}|\,\boldsymbol{n} = \sqrt{6}k\boldsymbol{n}$, with $|\boldsymbol{X}| = \sqrt{\boldsymbol{X} : \boldsymbol{X}}$ signifying the norm of a tensor $\boldsymbol{X}$, yields:

$$\lambda = \frac{1}{K^p}\boldsymbol{n} : \dot{\boldsymbol{s}} \tag{5}$$

$$K^p = -\left|\frac{\partial f}{\partial\boldsymbol{\sigma}}\right|^{-1}\left(\frac{\partial f}{\partial k}\bar{k} + \frac{\partial f}{\partial\boldsymbol{\alpha}} : \bar{\boldsymbol{\alpha}}\right) = \sqrt{\frac{2}{3}}\bar{k} + \bar{\boldsymbol{\alpha}} : \boldsymbol{n} \tag{6}$$

where $K^p$ is the all-important plastic modulus and use of $\boldsymbol{n} : \bar{\boldsymbol{\alpha}} = \bar{\boldsymbol{\alpha}} : \boldsymbol{n}$ was made for the last member of Eq. (6). Notice that the plastic strain rate Eq. (4), does not affect the loading index and plastic modulus because the plastic strain does not enter Eq. (1), thus, it does not appear in the consistency condition, $\dot{f} = 0$. Eqs. (1)–(6) provide the complete set of equations for any IH and KH plasticity model with YS given by Eq. (1), and the various forms of such models depend exclusively on the choice of the functions $\bar{k}$ and $\bar{\boldsymbol{\alpha}}$.

With $\dot{e}^p_{eq} = \sqrt{(2/3)\dot{\boldsymbol{e}}^p : \dot{\boldsymbol{e}}^p}$ the equivalent plastic strain rate, the following most common and effective rate evolution equation is adopted for the IH rule:

$$\dot{k} = c_k\left(k_s - k\right)\dot{e}^p_{eq} = \langle\lambda\rangle\sqrt{\frac{2}{3}}c_k(k_s - k) = \langle\lambda\rangle\bar{k} \tag{7}$$

where use of Eq. (4) with $\dot{\boldsymbol{\varepsilon}}^p = \dot{\boldsymbol{e}}^p$ was made in deriving the third member of Eq. (7), $k_s$ denotes the saturation value (limit value) of $k$, and $c_k$ is a model constant controlling the pace at which $k$ approaches $k_s$. Notice that depending on whether $k_s > k$ or $k_s < k$ one has isotropic hardening (increase of $k$) or softening (decrease of $k$), respectively. Often $k_s$ is also made a function of other quantities, such as max strain amplitude, etc. It follows from Eq. (7) that $\bar{k} = \sqrt{2/3}\; c_k(k_s - k)$.

Before we introduce the BCD modification, it is expedient to present the format of AF KH used in this paper, which offers some elements of convenience for calibration purposes and helps in the subsequent connection with the BCD modification when applied to the BS model. Armstrong and Frederick (1966) in their seminal paper proposed the following rate equation for KH:

$$\begin{aligned}\dot{\boldsymbol{\alpha}} = \frac{2}{3}h\dot{\boldsymbol{\varepsilon}}^p - c\dot{e}^p_{eq}\boldsymbol{\alpha} = \langle\lambda\rangle\sqrt{\frac{2}{3}}c\left(\sqrt{\frac{2}{3}}\frac{h}{c}\boldsymbol{n} - \boldsymbol{\alpha}\right) = \langle\lambda\rangle\sqrt{\frac{2}{3}}c\left(\sqrt{\frac{2}{3}}\alpha^s\boldsymbol{n} - \boldsymbol{\alpha}\right)\\ = \langle\lambda\rangle\sqrt{\frac{2}{3}}c(\boldsymbol{\alpha}^s - \boldsymbol{\alpha})\end{aligned} \tag{8}$$

with $h$ and $c$ being the original AF parameters. Observe the use of $\alpha^s = h/c$ and $c$ in the final expression. The preference to use $\alpha^s = h/c$ instead of $h$, stems from the fact the $\boldsymbol{\alpha}^s = \sqrt{2/3}\alpha^s \boldsymbol{n}$ is the saturation or limit tensor towards which the back stress $\boldsymbol{\alpha}$ tends to converge with, at a pace defined by the constant $c$, such limit providing an easy to measure important material property; to the contrary, $h$ represents the more difficult to measure initial value of uniaxial plastic modulus (initial slope of stress-plastic strain curve).

The BCD modification of Eq. (8) yields:

$$\dot{\boldsymbol{\alpha}} = \langle \lambda \rangle \sqrt{\frac{2}{3}} c(\boldsymbol{\alpha}^s - [\delta \boldsymbol{\alpha} + (1-\delta)(\boldsymbol{n} : \boldsymbol{\alpha})\boldsymbol{n}]) = \langle \lambda \rangle \bar{\boldsymbol{\alpha}} \tag{9}$$

with the obvious definition of $\bar{\boldsymbol{\alpha}}$ following from the last two members of Eq. (9). $\delta$ is the relevant modification parameter whose role is to create a mixture of AF KH rule occurring for $\delta = 1$, and a Burlet and Cailletaud (1986) non-linear Prager type KH rule along $\boldsymbol{n}$, occurring for $\delta = 0$ and accounting for the fact $\boldsymbol{\alpha}^s = \sqrt{\frac{2}{3}}\alpha^s \boldsymbol{n}$. Substitution of $\bar{k}$ and $\bar{\boldsymbol{\alpha}}$ as defined by Eqs. (7) and (9), respectively, in Eq. (6), yields for plastic modulus after some simple algebra the expression:

$$K^p = \frac{2}{3} c_k (k_s - k) + \sqrt{\frac{2}{3}} c\,(\boldsymbol{\alpha}^s - \boldsymbol{\alpha}) : \boldsymbol{n} \tag{10}$$

Notice that $\delta$ disappears from the value of the plastic modulus and this is a great advantage because one can calibrate the plastic modulus value for UR or any radial ratcheting loading, and then calibrate the value of $\delta$ only for the KH direction that affects MR. Dafalias and Feigenbaum (2011) showed analytically that one must have $\delta > 0.5$ when the back stress $\boldsymbol{\alpha}$ lies on the implied limit or saturation surface with radius $\boldsymbol{\alpha}^s = \sqrt{\frac{2}{3}}\alpha^s \boldsymbol{n}$, for guaranteeing it will not “cross” it and yield unrealistic negative plastic modulus due to the negative value of the term $(\boldsymbol{\alpha}^s - \boldsymbol{\alpha}) : \boldsymbol{n}$ in the foregoing Eq. (10) for $K^p$, that occurs when $\boldsymbol{\alpha}$ is outside the surface with radius $\alpha^s$ and $\boldsymbol{n}$ is properly chosen. In addition, Dafalias and Feigenbaum (2011) proposed replacing the fixed BCD modification parameter $\delta$ with the variable ratio:

$$r = \frac{\sqrt{(3/2)\,\boldsymbol{\alpha} : \boldsymbol{\alpha}}}{\sqrt{(3/2)\,\boldsymbol{\alpha}^s : \boldsymbol{\alpha}^s}} = \frac{\alpha}{\alpha^s} \tag{11}$$

with $\alpha$, $\alpha^s$ the norms of $\boldsymbol{\alpha}$, $\boldsymbol{\alpha}^s$, respectively, measuring the proximity of the back stress to its saturation value lying on a saturation surface; naturally $r = 1$ when the back stress is on the saturation surface, hence, being greater than 0.5, it does not induce any negative plastic modulus ever as per the discussion preceding Eq. (11). The fact that $r$ varies, implies a variation of the mixture of the two KH rules, as explained after Eq. (9).

## 3. Bounding surface formulation with BCD modification

### 3.1. General formulation

The methodology for the formulation follows closely, but not identically, the one in Mahan et al. (2011) where the resulting constitutive model was named SANISTEEL, from the initial letters of Simple ANIsotropic STEEL, addressing mainly steel materials. Since the main theoretical novelty will be the use of the BCD modification while addressing all kinds of different metals, the adopted name for the present model will be SANIMETAL-BCD, even though the materials simulated in this work will belong to the Carbon Steel (CS) family. Another change from Mahan et al. (2011) is that in this paper an evolving BS for the YS back stress, instead of the stress, will be adopted, as already done for soils (Manzari and Dafalias, 1997; Dafalias and Manzari, 2004). Recall from the Introduction that Marquis (1979) interpreted the limit surface for the back stress implied in any AF model, as a corresponding fixed BS for such back stress.

Fig. 1 serves as the key illustration of the analytical description that follows, and one must automatically refer to this figure in the following. The YS, given analytically by Eq. (1), is shown as a circle

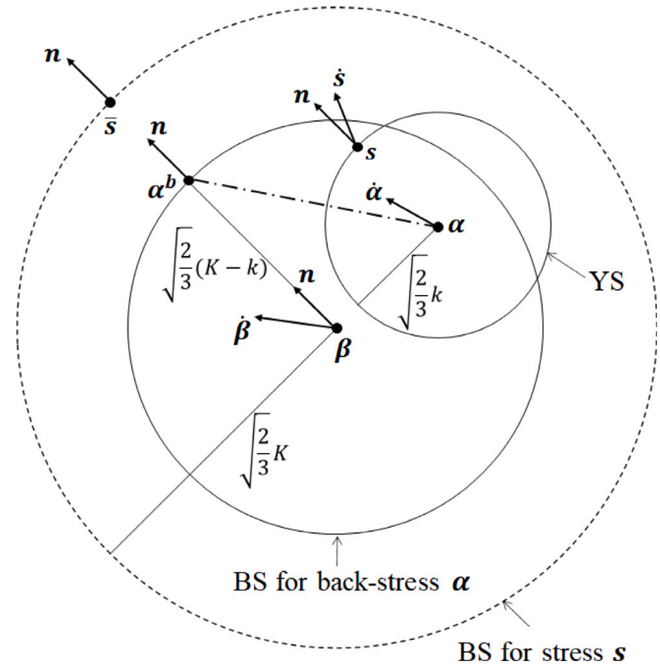


**Fig. 1.** Illustration of the concepts of YS, BS for the stress $\boldsymbol{s}$, BS for the back stress $\boldsymbol{\alpha}$, unit norm tensor $\boldsymbol{n}$ normal to YS at current stress $\boldsymbol{s}$, stress rate $\dot{\boldsymbol{s}}$, image back stress $\boldsymbol{\alpha}^b$, image stress $\bar{\boldsymbol{s}}$, and an indication of the KH rates $\dot{\boldsymbol{\alpha}}$ and $\dot{\boldsymbol{\beta}}$.

(sphere in deviatoric multiaxial stress space) of center $\boldsymbol{\alpha}$ and radius $\sqrt{2/3}k$. The current deviatoric stress tensor $\boldsymbol{s}$ and unit norm tensor $\boldsymbol{n}$, normal to the YS at $\boldsymbol{s}$, are also shown, as well as the imposed stress rate $\dot{\boldsymbol{s}}$. The classical BS for the stress is shown as a dashed circle of center $\boldsymbol{\beta}$ and radius $\sqrt{2/3}K$ on which the image stress $\bar{\boldsymbol{s}}$ is located along the radius with direction $\boldsymbol{n}$ emanating from $\boldsymbol{\beta}$. The BS for the back stress is analytically expressed by:

$$F = \frac{3}{2}\left(\boldsymbol{\alpha}^b - \boldsymbol{\beta}\right) : \left(\boldsymbol{\alpha}^b - \boldsymbol{\beta}\right) - (K-k)^2 = 0 \tag{12}$$

and shown in Fig. 1 as a solid line circle with same center $\boldsymbol{\beta}$ and radius the difference $\sqrt{2/3}(K-k)$ between the radii of BS for stress and YS. The image back-stress $\boldsymbol{\alpha}^b$ of the back-stress $\boldsymbol{\alpha}$, lies on the above BS and is located along the radius with direction $\boldsymbol{n}$ emanating from $\boldsymbol{\beta}$ as illustrated in Fig. 1, and analytically defined by:

$$\boldsymbol{\alpha}^b = \boldsymbol{\beta} + \sqrt{\frac{2}{3}}(K-k)\,\boldsymbol{n} \tag{13}$$

This variable $\boldsymbol{\alpha}^b$ is the tensor with which the back stress $\boldsymbol{\alpha}$ of the YS converges. Notice the difference of $\boldsymbol{\alpha}^b$ from its counterpart $\boldsymbol{\alpha}^s = \sqrt{2/3}\alpha^s\boldsymbol{n}$ entering Eqs. (7) and (9), had no BS been introduced. The isotropic hardening of the BS follows the scheme of IH for the YS as per Eq. (7) and reads:

$$\begin{aligned}\dot{K} - \dot{k} &= \left[C_K(K_s - K) - c_k(k_s - k)\right]\dot{e}^p_{eq} = \langle\lambda\rangle\sqrt{\frac{2}{3}}\left[C_K(K_s - K) - c_k(k_s - k)\right] \\ &= \langle\lambda\rangle(\bar{K} - \bar{k})\end{aligned} \tag{14}$$

where $K_s$ denotes the saturation value (limit value) of $K$, $C_k$ is a model constant controlling the pace at which $K$ approaches $K_s$, and from the last two members of Eq. (14) clearly follows that $\bar{k} = \sqrt{2/3}c_k(k_s - k)$ and $\bar{K} = \sqrt{2/3}C_k(K_s - K)$.

Postponing for later the definition of the KH of the BS by means of the analytical expression of the rate of its center $\boldsymbol{\beta}$, we focus on the modification of the KH for the back stress, center of the YS, in the presence of the BS in association with the BCD modification, i.e., on the modification of Eq. (9). First and foremost the $\boldsymbol{\alpha}^b$, as given by Eq. (13), must substitute for $\boldsymbol{\alpha}^s$ in both Eqs. (8) and (9). Assuming next radial loading from zero along a fixed direction $\boldsymbol{n}$, observe first that Eq. (9), the KH rule with the BCD modification, becomes identical to AF KH as per Eq. (8), because $\boldsymbol{\alpha}$ develops along $\boldsymbol{n}$ and consequently all the terms with $\delta$ cancel out. Because $\boldsymbol{\alpha}^b$ lies on a BS, it evolves also along $\boldsymbol{n}$ due to IH and KH of the BS, as eloquently implied by taking the rate of Eq. (13), providing a moving "target" for the evolving $\boldsymbol{\alpha}$. Because the rate of $\boldsymbol{\alpha}$ depends on the distance $\boldsymbol{\alpha}^b - \boldsymbol{\alpha}$ as per Eq. (8) resulting from Eq. (9) for radial loading along $\boldsymbol{n}$ (recall substitution of $\boldsymbol{\alpha}^b$ for $\boldsymbol{\alpha}^s$ in the foregoing equations), it will eventually approach the $\boldsymbol{\alpha}^b$ sufficiently close to have a small enough distance from it that necessarily causes the same rate of $\boldsymbol{\alpha}$ with that of $\boldsymbol{\alpha}^b$ along $\boldsymbol{n}$. Thus, the back stress $\boldsymbol{\alpha}$ may never be able to reach the BS at $\boldsymbol{\alpha}^b$ as it is supposed to do, unless the $\boldsymbol{\alpha}^b$ stops evolving in the case of a fixed BS, as it happens for the fixed limit surface of a classical AF model. The remedy of this unrealistic eventuality, which did not exist for the simple BCD modification of AF as per Eq. (9) where $\boldsymbol{\alpha}^s$ was fixed, is very simple. First, the rate of $\boldsymbol{\alpha}^b$ is obtained by taking the rate of Eq. (13) and using Eq. (14). Second, one can modify Eq. (9) by just adding the rate of $\boldsymbol{\alpha}^b$ to the rate of $\boldsymbol{\alpha}$ while substituting for the fixed $\delta$ a variable BCD modification parameter $r_\alpha$ (to be defined in the sequel), and write:

$$
\begin{aligned}
\dot{\boldsymbol{\alpha}} &= \dot{\boldsymbol{\alpha}}^b + \langle\lambda\rangle\sqrt{\frac{2}{3}}c\left(\boldsymbol{\alpha}^b - \left[r_\alpha\boldsymbol{\alpha} + \left(1-r_\alpha\right)(\boldsymbol{\alpha} : \boldsymbol{n})\boldsymbol{n}\right]\right) \\
&= \dot{\boldsymbol{\beta}} + \sqrt{\frac{2}{3}}\left(\dot{K} - \dot{k}\right)\boldsymbol{n} + \langle\lambda\rangle\sqrt{\frac{2}{3}}c\left(\boldsymbol{\alpha}^b - \left[r_\alpha\boldsymbol{\alpha} + \left(1-r_\alpha\right)(\boldsymbol{\alpha} : \boldsymbol{n})\boldsymbol{n}\right]\right) \\
&= \langle\lambda\rangle\Bigg[\bar{\boldsymbol{\beta}} + \frac{2}{3}\left[C_K\left(K_s - K\right) - c_k\left(k_s - k\right)\right]\boldsymbol{n} \\
&\quad + \sqrt{\frac{2}{3}}c\left(\boldsymbol{\alpha}^b - \left[r_\alpha\boldsymbol{\alpha} + \left(1-r_\alpha\right)(\boldsymbol{\alpha} : \boldsymbol{n})\boldsymbol{n}\right]\right)\Bigg] \\
&= \langle\lambda\rangle\bar{\boldsymbol{\alpha}}
\end{aligned}
\tag{15}
$$

where for the KH of the BS the general expression $\dot{\boldsymbol{\beta}} = \langle\lambda\rangle\ \bar{\boldsymbol{\beta}}$ was assumed, the $\bar{\boldsymbol{\beta}}$ to be defined in the sequel, and where the $\bar{\boldsymbol{\alpha}}$ is clearly defined by the last two members of Eq. (15) as the quantity in brackets that is multiplied by $\langle\lambda\rangle$. In Fig. 1 $\dot{\boldsymbol{\alpha}}$ is shown schematically along a direction between $\boldsymbol{n}$ and $\boldsymbol{\alpha}^b - \boldsymbol{\alpha}$, as expected by the mixture of two kinds of KH implied by the BCD modification; the $\boldsymbol{\alpha}^b - \boldsymbol{\alpha}$ is indicated by a dashed–dotted line connecting $\boldsymbol{\alpha}$ and $\boldsymbol{\alpha}^b$.

The all-important plastic modulus $K^p$ is obtained by substitution of $\bar{k}$ from Eq. (7) and $\bar{\boldsymbol{\alpha}}$ from Eq. (15) in Eq. (10), yielding:

$$
K^p = \frac{2}{3}c_k\left(k_s - k\right) + \bar{\boldsymbol{\alpha}} : \boldsymbol{n} = \bar{\boldsymbol{\beta}} : \boldsymbol{n} + \frac{2}{3}C_K\left(K_s - K\right) + \sqrt{\frac{2}{3}}c\left(\boldsymbol{\alpha}^b - \boldsymbol{\alpha}\right) : \boldsymbol{n}
\tag{16}
$$

As expected, notice that the BCD modification parameter $r_\alpha$ of Eq. (15) disappears from Eq. (16) for the plastic modulus, indicating that the role of $r_\alpha$ is only to define the KH direction of the YS in reference to the KH of the BS as per Eq. (15). The IH of the YS does not appear in the last member of Eq. (16) for the plastic modulus but has its place in Eq. (15) for the updating of the YS back stress. Finally, compare Eq. (16) with Eq. (10) for the classical AF model with (or without) BCD modification; they are entirely different due to the BS role, such role becoming more prominent when the quantities $\bar{\boldsymbol{\beta}}$ and $c$ are defined as functions of the state in the sequel.

### 3.2. Three important and novel constitutive functions

Eq. (15) constitutes the main novel contribution of the present SANIMETAL-BCD model. It expresses the much sought-after KH of the YS in relation to the KH of the BS using a variant of the BCD modification, such variant depending on the constitutive function that yields the BCD modification parameter $r_\alpha$. In addition to the usual IH constants $c_k$, $k_s$, $C_k$, $K_s$ for YS and BS entering Eqs. (14) and (15), there are three remaining very important constitutive functions that must be specified for the application of Eq. (15) and the ensuing Eq. (16): the $c$, $\bar{\boldsymbol{\beta}}$ and $r_\alpha$. Each one will be addressed separately in the following.

#### 3.2.1. The function $c$

The first two terms of the last member of Eq. (16) express the bounding plastic modulus $\bar{K}^p$ obtained by the consistency condition applied to the BS for the stress (Mahan et al., 2011), when BS obeys KH and IH, respectively, for each term. Thus, Eq. (16) can be written as $K^p = \bar{K}^p + \sqrt{2/3}c(\boldsymbol{\alpha}^b - \boldsymbol{\alpha}) : \boldsymbol{n}$, which is the quintessential feature of any classical BS plasticity model, namely that the plastic modulus equals the bounding plastic modulus (on BS for stress) plus a projected along $\boldsymbol{n}$ "distance" $(\boldsymbol{\alpha}^b - \boldsymbol{\alpha}) : \boldsymbol{n}$ of the current back stress $\boldsymbol{\alpha}$ from its evolving image bounding value $\boldsymbol{\alpha}^b$ on the BS for back stress, multiplied by $\sqrt{2/3}c$. Observe that the aforementioned projection along $\boldsymbol{n}$ of the "distance" between back stress quantities, substitutes for the exactly equal projection along $\boldsymbol{n}$ of the "distance" $(\bar{\boldsymbol{s}} - \boldsymbol{s}) : \boldsymbol{n}$ between stress quantities of the classical BS development, as already mentioned (the $\bar{\boldsymbol{s}} - \boldsymbol{s}$ tensor can easily be visualized, but not shown, in Fig. 1). If the pre-multiplying quantity $c$ is fixed, the distance dependence is linear, resembling the linear dependence on the distance of $\boldsymbol{\alpha}$ from its saturation value $\boldsymbol{\alpha}^s$ in Eq. (10) for a typical AF model. However, a linear dependence is inadequate to simulate the stress–strain curves accurately, hence, a non-linear dependence on the distance will be introduced by means of the function $c$, along the lines of flexibility provided within the BS constitutive framework.

As early as in Dafalias (1975) and Dafalias and Popov (1976), it was recognized that the value of such distance at the initiation of a new plastic loading process plays a very important role in the determination of $c$. While in the aforementioned references the distances and BS were referring to stress, in the present development the BS and corresponding distances are related to the back stress and so must the corresponding initial values. Along the lines of models developed for soil plasticity (Manzari and Dafalias, 1997; Dafalias and Manzari, 2004) with BS for the back stress, the following definition of $c$ is proposed:

$$
c = \frac{h_0}{\sqrt{3/2}\langle(\boldsymbol{\alpha} - \boldsymbol{\alpha}_{in}) : \boldsymbol{n}\rangle}
\tag{17}
$$

In Appendix the difference of the denominator of Eq. (17) from the corresponding denominator in Dafalias and Popov (1976) and Mahan et al. (2011) where initial values refer to stress rather than back stress, is elaborated in detail.

The value of the parameter $h_0$ is normally fixed, but if a more sophisticated data set, like random cyclic loading or UR must be simulated, the original suggestion of Dafalias (1975) and Dafalias and Popov (1976) to render $h_0$ function of the initial distance $\delta_{in} = \sqrt{3/2}\left(\bar{\boldsymbol{s}}_{in} - \boldsymbol{s}_{in}\right) : \boldsymbol{n}_{in}$ between initial values of deviatoric stress $\boldsymbol{s}_{in}$ and its image stress $\bar{\boldsymbol{s}}_{in}$ on the BS in multiaxial space, projected on the initial value $\boldsymbol{n}_{in}$ of $\boldsymbol{n}$ is adopted, as:

$$
h_0 = \frac{a}{1 + b(\delta_{in}/\sigma_r)^m}
\tag{18}
$$

with $\sigma_r$ a reference normalization stress quantity, as for example the double radial "size" $2K$ of the BS for stress, or $2(K-k)$ of the BS for back stress; in this work, the value $2K$ was used. Eq. (18) introduces three constants $a$, $b$, $m$, for which closed-form analytical expressions in terms of specific measurements on the experimental stress–strain curves are obtained in Dafalias and Popov (1976) with additional examples in Behravesh and Dafalias (2022) and will not be repeated here. Since we are working in a formulation with BS for back stress instead of stress, $\delta_{in}$ should be given in terms of back stress quantities. Thus, accounting for Eq. (13) and the relations $\boldsymbol{s}_{in} = \boldsymbol{\alpha}_{in} + \sqrt{2/3}k_{in}\boldsymbol{n}_{in}$ and $\bar{\boldsymbol{s}}_{in} = \boldsymbol{\beta}_{in} + \sqrt{2/3}K_{in}\boldsymbol{n}_{in}$, one can easily show that $\delta_{in} = \sqrt{3/2}\left(\bar{\boldsymbol{s}}_{in} - \boldsymbol{s}_{in}\right) : \boldsymbol{n}_{in} = \sqrt{3/2}\left(\boldsymbol{\alpha}^b_{in} - \boldsymbol{\alpha}_{in}\right) : \boldsymbol{n}_{in}$, to be used in Eq. (18) for $h_0$.

### 3.2.2. The function $\bar{\boldsymbol{\beta}}$

This function defines the KH of the BS according to $\dot{\boldsymbol{\beta}} = \langle \lambda \rangle \bar{\boldsymbol{\beta}}$. One can use a simple linear Prager-type KH, or an AF KH with or without a BCD modification, or anything else one finds most appropriate. As mentioned in the introduction the special KH called the Dafalias/Ranjbari (DR) KH, was found by Hassan and Kyriakides (1992, 1994a) to be very appropriate for UR, because it induces a parallel translation of the bounds towards the direction of ratcheting in the uniaxial case, a feature that helps to simulate accurately UR, and it is therefore adopted here. The analytical expression for $\dot{\boldsymbol{\beta}}$ can be found in Mahan et al. (2011) and is rewritten below as:

$$\dot{\boldsymbol{\beta}} = \langle \lambda \rangle \left( \frac{2}{3} h_\beta \boldsymbol{n} + \frac{1}{2}\sqrt{\frac{2}{3}} c_\beta \left[ \sqrt{\boldsymbol{\beta} : \boldsymbol{\beta}}\, \boldsymbol{n} - \boldsymbol{\beta} \right] \right) = \langle \lambda \rangle \bar{\boldsymbol{\beta}} \tag{19}$$

introducing two constants $h_\beta$ and $c_\beta$ with an obvious definition of $\bar{\boldsymbol{\beta}}$ as the quantity in parentheses of the second member of Eq. (19) which is identical to Eq. (34a) of Mahan et al. (2011). Based on this definition the term $\bar{\boldsymbol{\beta}} : \boldsymbol{n}$ of Eq. (16) becomes $\bar{\boldsymbol{\beta}} : \boldsymbol{n} = (2/3)\, h_\beta + (1/2)\sqrt{2/3} c_\beta [\sqrt{\boldsymbol{\beta} : \boldsymbol{\beta}} - \boldsymbol{\beta} : \boldsymbol{n}]$, i.e., identical to Eq. (34b) of Mahan et al. (2011). In Fig. 2(c) of the foregoing reference, a graphic illustration of the DR KH response in uniaxial loading is presented, while Eq. (18a) of that same reference yields the uniaxial expression of the above Eq. (19). Upon monotonic loading it exhibits a linear hardening with slope $h_\beta$, while upon unloading and reloading in the opposite direction, the hardening becomes an AF non-linear type controlled by both constants $h_\beta$ and $c_\beta$ till again switches smoothly to linear hardening in the opposite direction. It is exactly this smooth interchange between linear and non-linear hardening that induces the parallel translation of the bounds in the direction of ratcheting, discovered and used by Hassan and Kyriakides (1992, 1994a) for better simulation of UR.

### 3.2.3. The function $r_\alpha$

As already mentioned, the $r_\alpha$ substitutes for the fixed BCD modification parameter $\delta$ that was replaced in Dafalias and Feigenbaum (2011) by the ratio $r$ which is defined in Eq. (11) for an AF model. In our approach, we will consider $r_\alpha$ a function of $r$, but now the latter must be redefined because the BS center $\boldsymbol{\beta}$ moves with KH, unlike the center of the implied limit or saturation surface in an AF model that stays fixed at the origin in stress space. The new $r$ definition reflects the proximity of the back stress $\boldsymbol{\alpha}$ to its bounding value $\boldsymbol{\alpha}^b$ on the BS, such proximity measured relatively to $\boldsymbol{\beta}$, thus, it is given by:

$$r = \sqrt{\frac{(\boldsymbol{\alpha} - \boldsymbol{\beta}) : (\boldsymbol{\alpha} - \boldsymbol{\beta})}{(\boldsymbol{\alpha}^b - \boldsymbol{\beta}) : (\boldsymbol{\alpha}^b - \boldsymbol{\beta})}} \tag{20}$$

A very simple power function of $r$ is proposed for the BCD modification parameter $r_\alpha$ as follows:

$$r_\alpha(r) = c_{r1} r^{c_{r2}} \tag{21}$$

introducing two constants $c_{r1}$, $c_{r2}$ with the only requirement $c_{r1} > 0.5$ at $r = 1$ so that $r_\alpha(1) = c_{r1} > 0.5$. This is necessary in order to avoid for the BCD modification the possible eventuality of the YS center crossing its BS and inducing softening due to a negative plastic modulus resulting from the last term of Eq. (16), as discussed after Eq. (10). The rigorous analytical proof of the foregoing is given in Dafalias and Feigenbaum (2011).

It is now important to investigate the effect of $r_\alpha$ on the YS backstress translation direction $\bar{\boldsymbol{\alpha}}$ defined in Eq. (15). It can be seen from Eq. (20) that $r$ takes values from 0 to 1, as $\boldsymbol{\alpha}$ varies from $\boldsymbol{\beta}$ to $\boldsymbol{\alpha}^b$, respectively. When $r = 0$, it follows from Eq. (21) that $r_\alpha = 0$ and the relative translation of the YS's center $\boldsymbol{\alpha}$ with respect to its image back stress $\boldsymbol{\alpha}^b$ on the BS, is along $\boldsymbol{\alpha}^b - (\boldsymbol{\alpha} : \boldsymbol{n})\boldsymbol{n}$ as per Eq. (15); this is a variation of a non-linear Prager-type KH suggested by Burlet and Cailletaud (1986), because from Eq. (13) the $\boldsymbol{\alpha}^b$ is not along $\boldsymbol{n}$, as it was the case for $\boldsymbol{\alpha}^s$ in Eq. (9) had it been a BCD modification for a typical AF KH. When $r = 1$ and for $c_{r1} = 1$, one has $r_\alpha = 1$, and the aforementioned relative translation is along $\boldsymbol{\alpha}^b - \boldsymbol{\alpha}$, i.e., a KH of the AF or Mroz type. If the $c_{r1}$ is not equal to 1, then at $r = 1$ one has $r_\alpha = c_{r1}$ which yields a variation of the non-linear AF KH rule for the relative translation of $\boldsymbol{\alpha}$ with respect to $\boldsymbol{\alpha}^b$. Therefore, the effect of the function $r_\alpha$ on the direction of the relative YS center translation with respect to its image back stress $\boldsymbol{\alpha}^b$ is very significant, and essentially the $r_\alpha$ defines this direction as an interpolation between the aforementioned directions of a variation of a non-linear Prager KH rule when $r = 0$ and a variation of the non-linear AF KH rule when $r = 1$. The absolute translation $\bar{\boldsymbol{\alpha}}$ is also affected by the KH rule chosen for the BS, namely the tensor $\bar{\boldsymbol{\beta}}$, as well as by the IH of both YS and BS yielding a component along $\boldsymbol{n}$, as per the first two terms in the brackets of the fourth member of Eq. (15), respectively.

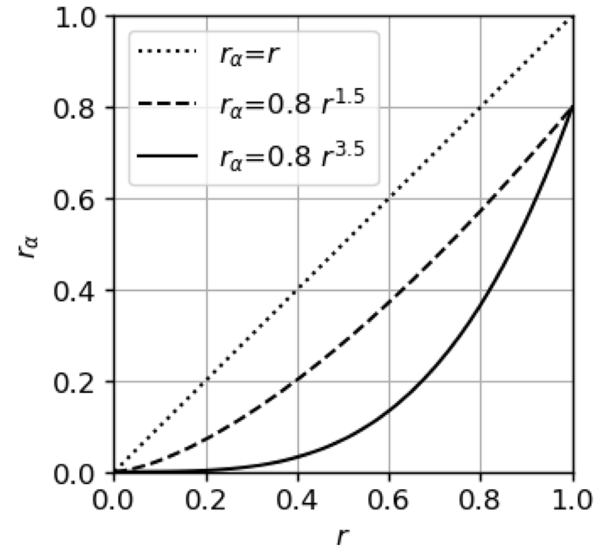


**Fig. 2.** The power law function for $r_\alpha$ to show how the weighting between AF and Prager KH can vary with the choice of parameters.

It is now clear that the use of $r_\alpha$, as the modification parameter, rather than $r$ or a fixed $\delta$, allows for a more flexible interpolation of the variations of the nonlinear Prager and AF KH rules as per Eq. (15). In Fig. 2 the variation of the "interpolating" BCD modification parameter $r_\alpha$ with $r$ is shown for various choices of the constants $c_{r1}$, $c_{r2}$ including the case of $c_{r1} = c_{r2} = 1$, namely the case where $r_\alpha(r) = r$. Based on attempted simulations for these various choices it was concluded that ratcheting would be better predicted if the direction of $\bar{\boldsymbol{\alpha}}$ is closer to $\boldsymbol{n}$ for a larger part of each cycle after the initiation of a new loading process (load reversal). It means that $r_\alpha$ must be close to 0 for a wider initial part of the range in the [0, 1] $r$ domain, after the loading reversal, compared to what could be achieved with the simple $r_\alpha = r$ equation. Accounting for the fact $0<r<1$, this can be achieved with the power function $r_\alpha(r) = c_{r1} r^{c_{r2}}$ with $c_{r2} > 1$, and the larger the $c_{r2}$ is, the more pronounced this effect is. This is illustrated in Fig. 2 by the dashed line with $c_{r2} = 1.5$ against the solid line with $c_{r2} = 3.5$, where there is a larger range where $r_\alpha$ is near zero for the latter case.

## 4. Model calibration

Uniaxial and multiaxial ratcheting simulations and comparisons with published experimental data are presented in the next section. Those experiments were published in Hassan and Kyriakides (1992), Hassan et al. (1992) and Corona et al. (1996) and performed on three different carbon steels, namely CS1018, CS1020 and CS1026, respectively. The input model constants for each material, together with some notes for their determination, are presented in this section.

**Table 1**
Model constants for three steel materials, CS1018, CS1020 and CS1026.

| Equation | Symbol | CS1018 | CS1020 | CS1026 |
|---|---|---|---|---|
| – | $\nu$ | 0.33 | 0.33 | 0.33 |
| – | $E$ | 26320 ksi | 25125 ksi | 26320 ksi |
| 1 | $k_{in}, k_s$ | 23, 23 ksi | 25, 25 ksi | 19, 20.2 ksi |
| 12 | $^*K_{in}, K_s$ | 43, 43 ksi | *60.15, 60.15 ksi | 38.5, 38.5 ksi |
| 7 | $c_k$ | 0 | 0 | 250 |
| 14 | $C_k$ | 0 | 0 | 0 |
| 18 | $a, b, m$ | 91100, 27, 2 | 146200, 40, 3 | 71100, 27, 2 |
| 19 | $c_\beta$ | 30 | 73.5 | 15 |
| 19 | $h_\beta$ | 650 | 700.35 | 300 |
| 21 | $c_{r1}, c_{r2}$ | 0.8, 3.5 | 0.8, 3.5 | 0.8, 3.5 |

* In few sets of uniaxial experiments, an adjusted $K_{in}$ was used. In those cases, the adjusted values are reported explicitly in the relevant locations.

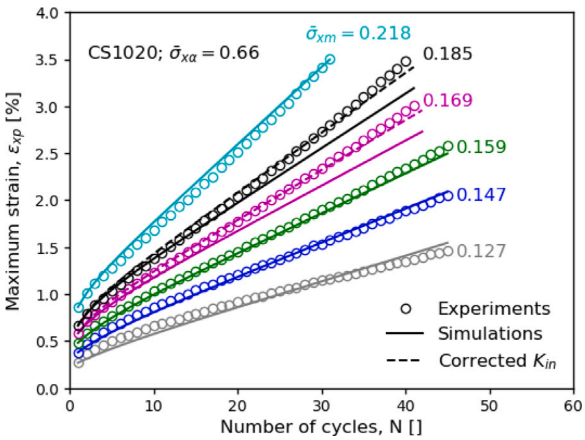


**Fig. 3.** Uniaxial ratcheting experiments on CS1020. Same applied stress, varying mean stress.

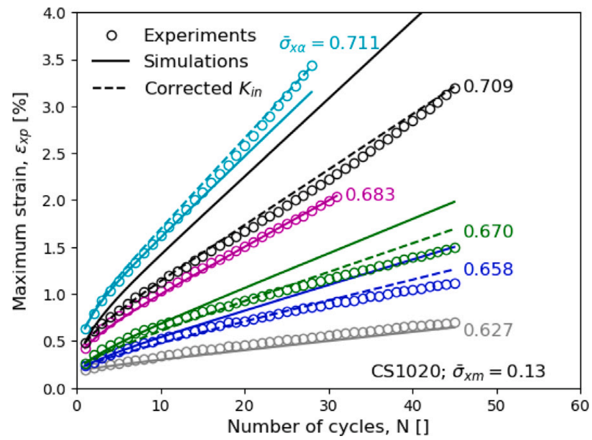


**Fig. 4.** Uniaxial ratcheting experiments on CS1020. Same mean stress, varying applied stress.

Table 1 presents the model constants used for the simulations of both UR and MR for all three materials. In all the experiments, the specimens were cyclically stabilized by strain symmetric cycles in the range of $\pm 1\%$. For details, the reader is referred to the introduction section of Hassan and Kyriakides (1992), Hassan et al. (1992) and Corona et al. (1996). This cyclic stabilization process was not explicitly simulated in either the above references or here, and the simulations start with cyclic ratcheting from the stabilized state of each specimen. The model constants for UR are derived based on the stabilized strain symmetric cycles results, thus, they reflect the stabilized state of the material. Hassan and Kyriakides (1992), Hassan et al. (1992) and Corona et al. (1996) provided such material constants for a Dafalias/Popov bounding surface plasticity model, with the plastic modulus resulting from the Dafalias/Ranjbari KH for the BS, while an AF KH direction was used independently for the YS (see detailed comments made in Introduction). These model constants constitute a basis for a trial-and-error process of constants determination for the present model because for uniaxial conditions the two formulations are very close to each other, and the constants end up being the same or slightly modified.

The elastic Young's modulus $E$ can be easily measured from the slope of the elastic stress–strain curve of the stabilized cycle. A single Poisson's ratio $\nu = 0.33$ is used for all three carbon steels, following the proposition of Hassan and Kyriakides (1992) and Hassan et al. (1992). The initial value $k_{in}$ of the size of the YS that corresponds to the initial yield stress point in uniaxial loading, is measured approximately at the smooth transition from linear elastic to curved elastoplastic stress–strain curve. The initial value $K_{in}$ of the size of the BS can be measured approximately as the image stress point of the initial yield stress point on the bound, such bound representing the significantly "slower" non-linear part of the stress–strain curve with which the stress merges eventually upon continual loading. No isotropic hardening of the YS and BS are applied for the materials CS1018 and CS1020, thus, the constants $c_k$, and $c_K$ of Eqs. (7) and (14), respectively, are set equal to zero, and the saturation values $k_s$ and $K_s$ of Eq. (14) are set equal to their initial values, as reported in Table 1, and plotted with dashed lines in Figs. 3 and 4. For CS1026 a small IH was introduced only for the YS, because it was found that a very small increase in the size of the YS (from $k_{in} = 19$ ksi to $k_s = 20.2$ ksi) improves the simulations, especially for UR; correspondingly a value of $c_k = 250$ was used. The saturation value of $K_s$ is set equal to its initial value as reported in Table 1. The calibration of $k_s$ and $c_k$ was done by optimizing the results for the three UR tests presented in Fig. 6.

The constants $a$, $b$ and $m$ of Eq. (18) determine how the parameter $h_0$ changes, which controls the curvature of the non-linear part of the stress–strain curve, as a function of a measure of the initial distance in stress space between stress and its image on the BS for stress at the initiation of a new loading process, that has been observed to strongly affect the shape of the curve. Instead of using the available closed-form analytical expressions for these constants that require special measurements as mentioned after Eq. (18), it was decided to use a trial-and-error process to define an optimum shape for the highly non-linear part of the stress–strain curve before the stress merges with the image-stress on the bound. This was facilitated by the simple numerical implementation of the model in uniaxial loading and the knowledge of the effect $h_0$ has on the curve shape. For the CS1020 material, the values for the $a$, $b$ and $c$ constants provided in Hassan and Kyriakides (1992) for the Dafalias/Popov model was not changed, since they were the optimum values for the UR simulations of Fig. 3. Hassan and Kyriakides (1992) and Corona et al. (1996) proposed $a = 71000$, $b = 27$, and $c = 2$ for both CS1018 and CS1026 materials. Those parameters were used in this work for the CS1026 UR and MR tests. Since there are no UR CS1018 tests available to use for $a$, $b$, and $c$, $a$ was slightly modified to $a = 91000$, to improve the response in the three simulated CS1018 MR experiments of Fig. 23, while keeping $b$ and $c$ as reported in Hassan and Kyriakides (1992).

The constants $h_\beta$ and $c_\beta$ for the kinematic hardening of the BS are determined by trying to optimize the simulations of the UR response. The value of $h_\beta$ that yields a linear KH, reflects the slope of the bound in stress–strain space, thus, the higher its value is the smaller will be the parallel translation of the bound along the direction of ratcheting and, hence, the larger the number of cycles to reach a certain value of accumulated strain. A similar conclusion applies to the constant $c_\beta$ that in conjunction with $h_\beta$ controls the AF type non-linear KH for the BS, in reverse loading. For each material, one UR experiment is needed to optimize the values of $h_\beta$ and $c_\beta$. For the CS1020 material, the optimization was performed against the result of the test with $\sigma_{xm} = 0.159$ (Fig. 3). For the CS1026 material, the optimization was performed against the result of the test with $\sigma_{xm} = 0.225$. Since there are no UR CS1018 tests available, the optimization was done for all three MR tests of Fig. 23.

For the power law in Eq. (21), defining the BCD weighting parameter $r_\alpha$, the values $c_{r1} = 0.8$ and $c_{r2} = 3.5$ led to successful simulations for all the materials tested in this paper. One strain-symmetric cyclic MR test at constant pressure (in this case the case of $\epsilon_{xc} = 0.5\%$ of Fig. 3) was enough for their calibration, and then, the same values used successfully in all other UR and MR tests for all the materials. As shown in Fig. 2, these values maintain $r_\alpha$ close to zero for a large initial portion of the range $0 < r < 1$, thus, inducing a larger contribution of the variant of Prager non-linear KH type than that of an AF KH, on the relative overall KH of the YS relatively to the BS. Such initial predominance of Prager KH is necessary for the more accurate simulation of the MR response.

## 5. Model validation

The following notation is used in all subsequent plots for UR and MR:

- The $\sigma_x$ signifies the axial stress, $\sigma_{xm}$ signifies the mean values of $\sigma_x$ during cyclic loading, and $\sigma_{xa}$ half the peak-to-peak amplitude of the applied cyclic $\sigma_x$.
- The $\sigma_\theta$ signifies the circumferential stress, induced by internal pressure on thin-walled cylindrical samples. $\sigma_{\theta m}$ the mean value of the cyclic $\sigma_\theta$, and $\sigma_{\theta a}$ half the peak-to-peak amplitude of the cyclic $\sigma_\theta$.
- The $\epsilon_x$ signifies the axial strain, $\epsilon_{xc}$ half the peak-to-peak amplitude of the cyclic $\epsilon_x$, while the $\epsilon_{xp}$ signifies the peak $\epsilon_x$.
- The $\epsilon_\theta$ signifies the circumferential strain, and $\epsilon_{\theta p}$ signifies the peak $\epsilon_\theta$.
- A superposed bar on a stress symbol implies normalization by the yield limit.

### *5.1. Model validation in uniaxial ratcheting (UR)*

In this section, UR model simulations are compared with data from Hassan and Kyriakides (1992). The uniaxial ratcheting experiments are stress-controlled with varied amplitude of stress cycles and positive mean stress values. The mean stress and amplitude are normalized by the yield stress which is approximately $\sigma_o = 73$ ksi (based on a 0.2% strain offset yield stress) for CS1020, and $\sigma_o = 40.50$ ksi (based on the "plateau" stress) for CS1026.

#### *5.1.1. Material CS1020*

Two sets of UR experiments on CS1020 specimens are simulated in Figs. 3 and 4. In the first set, the cycling amplitude was kept constant, and the mean stress was varied (Fig. 3), while in the second set, the mean stress is constant, and the cycling amplitude is varied (Fig. 4). In both figures, the experimental data are presented with open circles, and the simulation results with colored dashed and solid lines. Before the discussion of the numerical simulation results and their comparison against the experimental data, two key aspects must be discussed; first, the applied correction of the predicted maximum axial strain, $\epsilon_{xp}$, at the first cycle, and second, the difference between the dashed and solid lines that are used in some cases for the numerical simulations in Figs. 3 and 4.

Regarding the first aspect, a direct specification of the maximum axial strain $\epsilon_{xp}$, that is generated at the end of the first cycle ($N = 1$) is used in the numerical simulations. Practically, this means that the very first point at $N = 1$ in all the curves of the numerical simulations of Figs. 3 and 4 is directly specified to match the corresponding experimental data point exactly. This same process was followed in Hassan and Kyriakides (1992), Hassan et al. (1992) and allowed them to focus on the predicted ratcheting rate after the first cycle ($N > 1$). The reason is that the symmetric cyclic stabilization process of the sample prior to ratcheting is not explicitly simulated, and consequently, the initial state of the material at the start of ratcheting is unknown. Had the stabilization process been simulated, it would have produced slightly different initial points at the end of the first ratcheting cycle than what is shown in the data due to model error in simulating the stabilization and the first cycle.

Regarding the second aspect, notice that there are cases where the numerical simulation results are presented with both solid and dashed lines for the same test (e.g., the purple solid and dashed lines for the case $\bar{\sigma}_{xm} = 0.169$ in Fig. 3). When the numerical simulation results are with solid lines, the model constants are those in Table 1. When a dashed line is used for a simulation, the results with those constants did not match well the experimental data and an adjustment of the value of $K_{in}$ only (single parameter adjustment) is applied for higher model accuracy. More specifically, in Fig. 3, the tests with $\bar{\sigma}_{xm} = 0.169$ and 0.185 are also simulated with a slightly adjusted $K_{in} = 59.65$ ksi value compared to $K_{in} = 60.15$ ksi in Table 1, and plotted with dashed lines. In Fig. 4, the tests with $\bar{\sigma}_{xa} = 0.658$, 0.670, 0.709 and 0.711 are also simulated with adjusted $K_{in} = 60.912$, 60.912, 62 and 59.5 ksi values, respectively, and plotted with dashed lines. It is worth noting that Hassan and Kyriakides (1992, 1994a) reported the results of their simulations with only adjusted, when needed, values of $K_{in}$. In this work, the results with both adjusted and non-adjusted unique $K_{in}$ values, the latter given in Table 1, are presented for completeness.

The results in Fig. 3 suggest that the model predicts with high accuracy the UR. Moreover, it successfully considers the effect of the applied mean stress, since it predicts with acceptable accuracy the ratcheting rate for the 6 tests of varying mean stress in Fig. 3, with a single set of model constants (solid lines). When the adjusted value of $K_{in}$ is applied for the cases of $\bar{\sigma}_{xm} = 0.169$ and 0.185 (dashed lines), the accuracy is improved and agreement between the predictions and the experimental data is excellent.

Before we address the results of Fig. 4, it is instructive to clarify the three stages of a typical stress–strain relationship in a simulation by the BS model, namely, the linear elastic loading (Stage 1, $f < 0$ and $F < 0$); the non-linear elastoplastic loading with axial stress on the YS but within the BS (Stage 2, $f = 0$ and $F < 0$); and the non-linear elastoplastic loading with axial stress on the YS and on the BS (Stage 3 with $f = 0$ and $F = 0$). In the case of the UR experiments of Fig. 4, if the maximum axial stress to be applied $\sigma_x = \sigma_{xm} + \sigma_{xa} > k_{in}$ then Stage 2 is initiated, and if $\sigma_x = \sigma_{xm} + \sigma_{xa} > K_{in}$ Stage 3 is initiated because $\beta$ has a significant smaller value compared to $K_{in}$ and the stress (and thus the YS) reaches the image stress (and thus the BS) when $\sigma_x = K_{in} + \beta$. Stage 1 is always simulated after the initiation of a new loading event. Clearly the same increment of axial stress $d\sigma_x$ acting during each of the three stages would cause a significantly larger increment of axial strain $d\epsilon_x$ in Stage 3, compared to Stage 2 and 1, in that order. This can be visualized by looking at the initial loading part of the simulated Stable

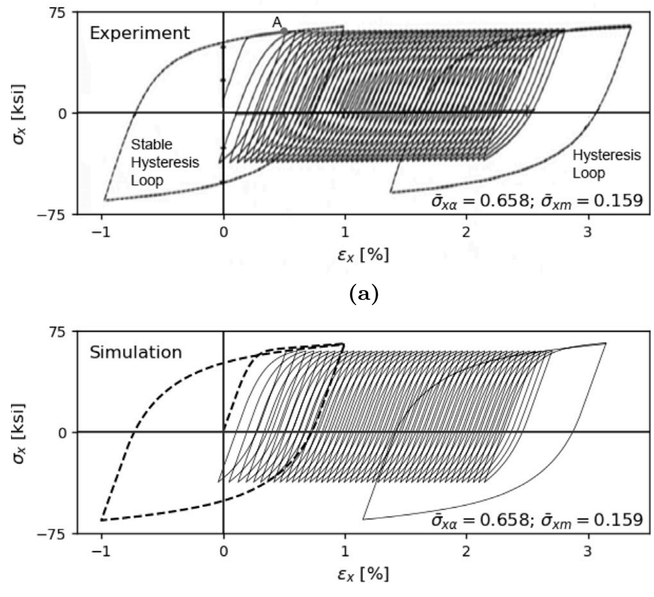


**Fig. 5.** Stress–strain response of CS1020 in uniaxial ratcheting. (a) Experiment after Hassan and Kyriakides (1992); (b) Simulation.

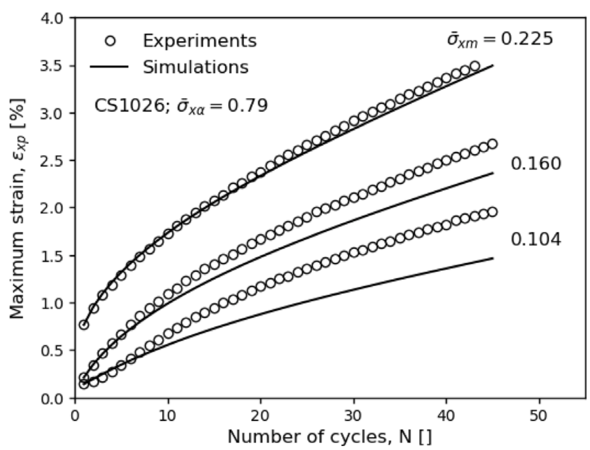


**Fig. 6.** Uniaxial ratcheting on CS1026. Constant applied stress. Data after Hassan and Kyriakides (1992).

Hysteresis Loop of Fig. 5(b) (black dashed line), where the slope of the stress–strain curve is much flatter just before unloading (Stage 3).

Addressing now the results of Fig. 4, let us focus on the cases of $\bar{\sigma}_{xa} = 0.627$, 0.658, 0.670 and 0.683 (gray, blue, green, and purple lines, respectively), where the maximum applied axial stress $\sigma_x = \sigma_{xm} + \sigma_{xa}$ is 55.26, 57.52, 58.4 and 59.34 ksi, respectively, lower than the calibrated $K_{in} = 60.15$ ksi (Table 1), hence, also $\sigma_x = \sigma_{xm} + \sigma_{xa} < K_{in} + \beta$. The simulated stress–strain relationship, in all the ratcheting cycles, is characterized by loading Stages 1 and 2 (linear elastic, and non-linear elastoplastic on the YS but within the BS) and thus the model did not predict as large increments of strains as it would had Stage 3 been activated, as explained before. This simulated response was qualitatively accurate with what was observed in the experiments, and thus those cases were simulated with adequate accuracy when the non-adjusted common $K_{in}$ is used (solid lines). When a small adjustment of $K_{in}$ is applied in the cases of $\bar{\sigma}_{xa} = 0.658$ and 0.670 the accuracy increased (dashed lines), not because the response is qualitatively different by entering for example in the large strain regime of Stage 3, but because the ratcheting slope is slightly improved within each cycle at Stage 2 by making the distance of the current axial stress to the image stress slightly larger in average.

In the last two cases of $\bar{\sigma}_{xa} = 0.709$, 0.711, the maximum axial stress reached in each of the experiments is 61.247 and 61.393 ksi, respectively. When those two experiments are simulated, the maximum applied axial stress per cycle is larger than the calibrated $K_{in} = 60.15$ ksi. Thus, in both cases, the model predicts large strain increments since part of loading is characterized by Stage 3, and thus, significantly larger accumulated strain at the end of each cycle is predicted, as demonstrated by the black and cyan solid lines in Fig. 4 for the cases of $\bar{\sigma}_{xa} = 0.709$, and 0.711, respectively. For the $\bar{\sigma}_{xa} = 0.711$ case (cyan open circles), the simulation results are in good agreement with the experimental results, and the simulation of large strain increments within each cycle (loading Stage 3) explains the steep slope of the cyan experimental and numerical curves. A small adjustment to the value of $K_{in}$ (dashed cyan line) improves the slope of the numerical curve not because the response gets qualitatively different, but by improving the stress–strain curve within each cycle by making the distance of the current axial stress to the image stress slightly larger in average. However, in the case of $\bar{\sigma}_{xa} = 0.709$, the simulation with non-adjusted $K_{in}$ (black solid line) over-predicts the accumulated total axial strain compared to the corresponding experiment, due to the fact that the model predicts large total stains within each cycle (loading Stage 3). However, this is not observed in the experimental results and thus, a significant adjustment (increase) of $K_{in} = 62$ ksi was needed to improve accuracy (dashed black line in Fig. 4), by practically forcing the elastoplastic response of the model to remain within Stage 2, i.e. the total applied axial stress 61.247 to remain smaller than $K_{in} = 60.15$ ksi. Note that Hassan and Kyriakides (1992) also applied similar adjustments to $K_{in}$ to increase the accuracy of the Dafalias/Popov BS model in their work.

A full experimental stress–strain curve for uniaxial ratcheting is plotted in Fig. 5(a), taken from Hassan and Kyriakides (1992), and its simulation is shown in Fig. 5(b). In the experiment, the CS1020 specimen was first cyclically stabilized by strain-symmetric cyclic loading of 1% axial strain amplitude. During cyclic stabilization, it exhibited cyclic softening (Hassan and Kyriakides, 1992) that is not simulated and presented in this work as explained in Section 4. When the specimen was stabilized, and cyclic softening finished, the specimen exhibited a stable hysteresis loop under strain-symmetric cyclic loading, which is indicated in Fig. 5(a) for the experiment and simulated in Fig. 5(b) with good accuracy (black dashed line). After the stabilization process, 45 cycles of UR were applied, with $\bar{\sigma}_{xa} = 0.658$ and $\bar{\sigma}_{xm} = 0.159$. At the end of UR another strain-symmetric cycle of the same amplitude with the stabilized loop was applied and is indicated as Hysteresis Loop in Fig. 5(a) and simulated in Fig. 5(b). The maximum accumulated axial strain in the experiment after 45 UR cycles is approximately 2.6% and the model predicts it with high accuracy, as can be seen in Fig. 5(b). The model can simulate all the features of this complicated loading history, and the numerical results compare very well with the experimental data.

### 5.1.2. Material CS1026

Nine additional UR experiments are simulated in this section and compared with experimental data on CS1026 presented in Hassan and Kyriakides (1992). In those experiments, a single set of model constants (including a single $K_{in}$) is used, as presented in Table 1. Fig. 6 presents the simulations and experimental data for three tests with the same cyclic amplitude but varying mean stress. The model shows good accuracy compared to the experimental data, except for the simulation of the experiment with the low $\bar{\sigma}_{xm} = 0.104$, which is significantly less accurate than the other two. Fig. 7 presents four tests with constant mean stress and varying cyclic amplitude. With a single set of parameters, the model shows good accuracy for the three tests, except the test when $\bar{\sigma}_{xa} = 0.771$, where it under-predicts significantly the maximum accumulated strain per cycle.

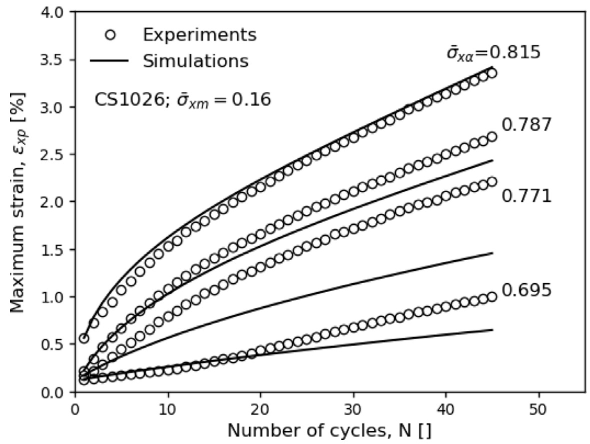


**Fig. 7.** Uniaxial ratcheting on CS1026. Constant mean stress. Hassan and Kyriakides (1992).

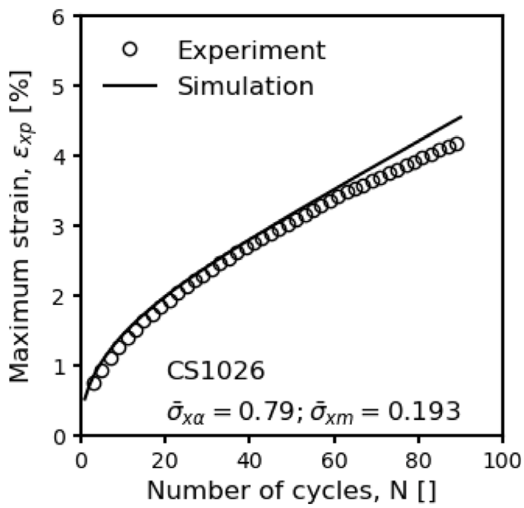


**Fig. 8.** Uniaxial ratcheting on CS1026 with a large number of cycles. Data after Hassan and Kyriakides (1992).

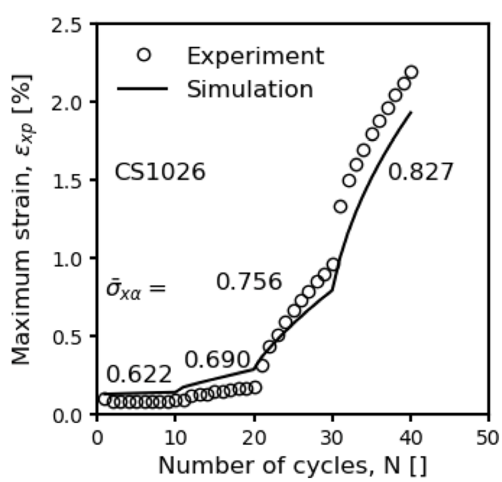


**Fig. 9.** Uniaxial ratcheting on CS026 with varying axial stress amplitude. Hassan and Kyriakides (1992).

Fig. 8 presents the experimental data and numerical simulations of a UR test on CS1026 with $\bar{\sigma}_{xa} = 0.79$ and $\bar{\sigma}_{xm} = 0.193$, and a large number of cycles ($N = 90$). These results suggest that the model can be very accurate even when a high number of cycles are applied. Fig. 9 presents the experimental data and numerical simulations of a UR with varying $\bar{\sigma}_{xa}$ during the test and mean normalized applied stress $\bar{\sigma}_{xm} = 0.16$. The agreement between the simulation and experimental data is very good. The full stress–strain relationship of this simulation and the comparison with the experiment is presented in Fig. 10.

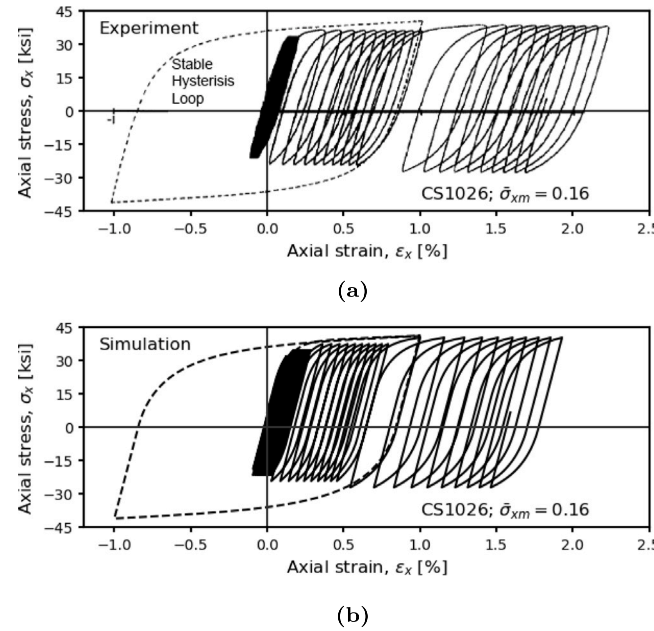


**Fig. 10.** Stress–strain relationship in uniaxial ratcheting with varying applied axial stress for CS1026. Applied stress history of Fig. 9. (a) Experiment after Hassan and Kyriakides (1992) (b) Simulation.

### 5.2. Model validation in multiaxial ratcheting (MR)

In this section, multiaxial ratcheting simulations are compared with experimental data on CS1018 and CS1026 specimens, reported in Hassan et al. (1992) and Corona et al. (1996). Six simulated loading histories are illustrated in Fig. 11, all in the space of the axial strain $\varepsilon_x$, versus circumferential stress $\sigma_\theta$, which is induced by pressure. The loading types of Fig. 11 can be described as follows: (1) axial strain-symmetric cycling at constant pressure, (2) inclined path, positive slope, (3) inclined path, negative slope, (4) bowtie path, (5) reverse bowtie path, and (6) hourglass path. Both CS1018 and CS1026 specimens are tested after a cyclic stabilization process, as explained in the uniaxial section. In the simulations, only the multiaxial ratcheting stages are simulated, but the stabilized state of the materials is reflected in the chosen model constants and simulations are adjusted such that the initial point matches that seen experimentally, as explained in the uniaxial section, to account for any previous loading.

#### 5.2.1. Material CS1026

The model constants for the multiaxial ratcheting simulations are the same as those used for CS 1026 uniaxial ratcheting simulations and are presented in Table 1. Fig. 12 presents the experimental data and numerical simulations for four axial strain-symmetric cycling tests at constant pressure (Type 1 in Fig. 11), for the same applied axial strain amplitude of $\varepsilon_{xc} = 0.5\%$ at various circumferential stresses $\sigma_\theta$, each one obtained by a corresponding constant internal pressure of the tubular specimen. In Fig. 12, as well as in all subsequent figures, the stress quantities are normalized by the yield stress value, hence, the bar over the stress symbol $\bar{\sigma}$. Fig. 13 presents the experimental data and

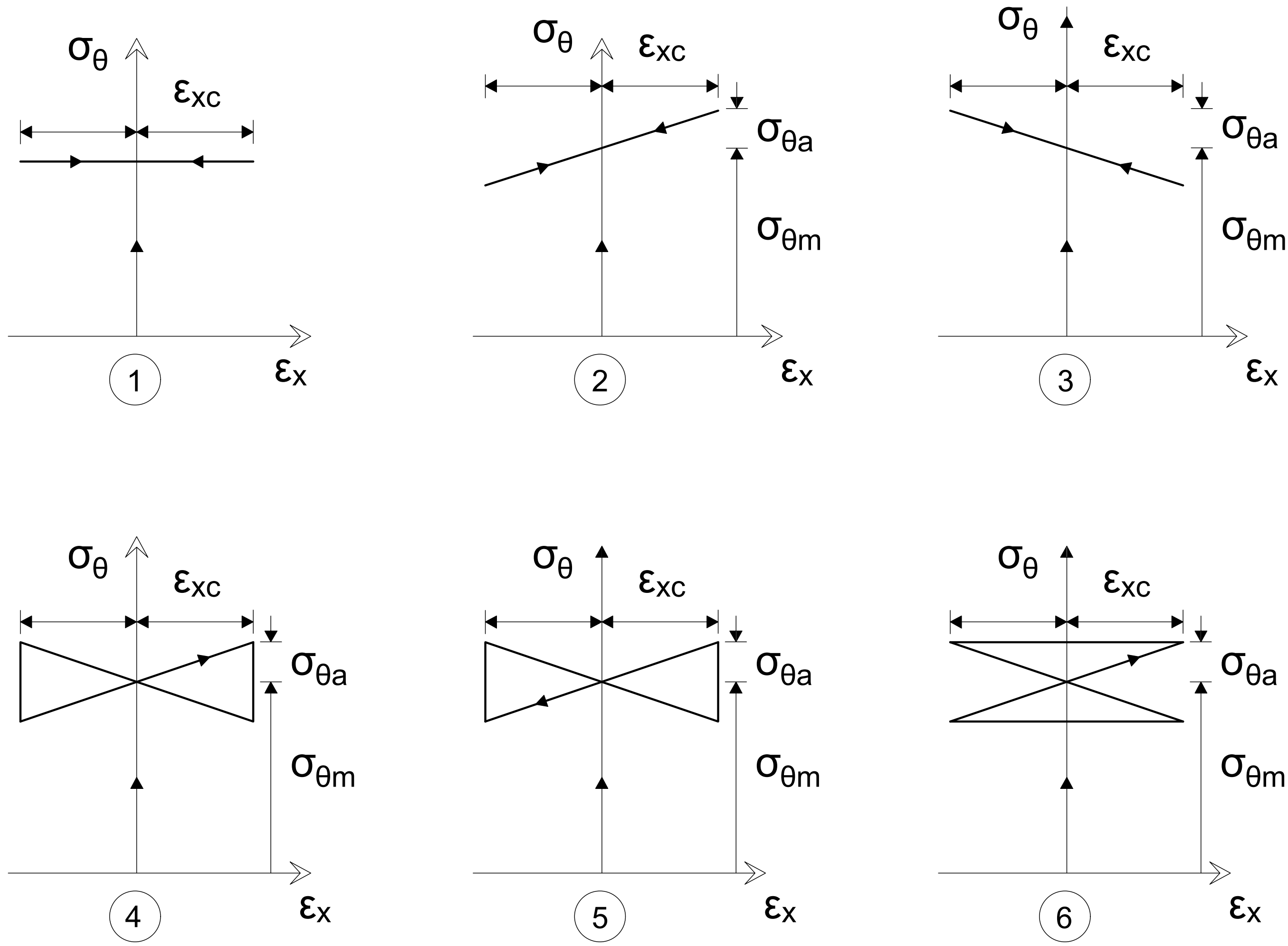


**Fig. 11.** Cycling types of loading histories (after Corona et al., 1996).

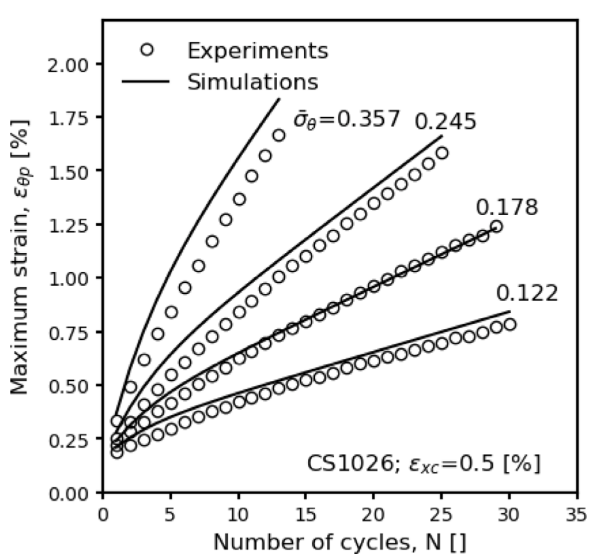


**Fig. 12.** Axial strain-symmetric cycling at constant pressure. Type 1 of Fig. 11. Constant applied axial strain across tests. Material CS1026. Data after Hassan et al. (1992).

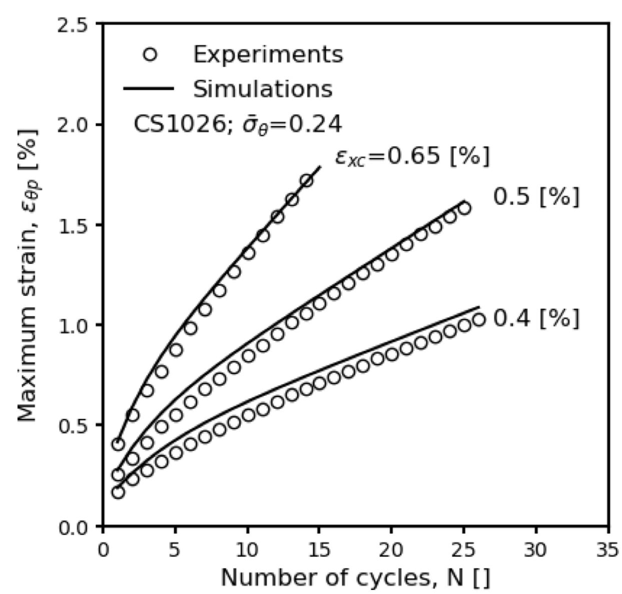


**Fig. 13.** Axial strain-symmetric cycling at constant pressure. Type 1 of Fig. 11. Constant applied circumferential stress across tests. Material CS1026. Data after Hassan et al. (1992).

numerical simulations for three axial strain-symmetric cycling tests at constant pressure (again Type 1 in Fig. 11), but now with the same $\bar{\sigma}_\theta = 0.24$ at various axial strain amplitudes, $\varepsilon_{xc}$. Fig. 14 presents the experimental data and simulation of the same Type 1 loading, with

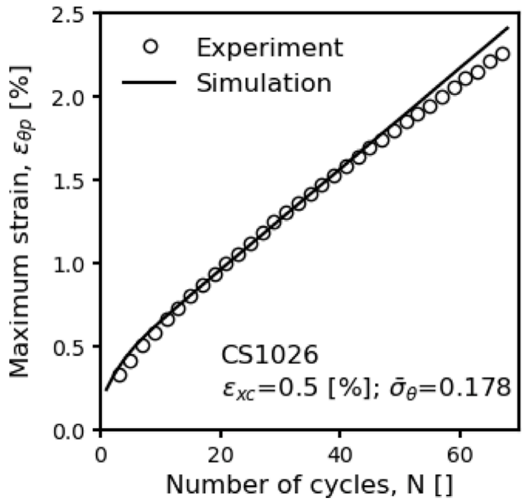


**Fig. 14.** Axial strain-symmetric cycling at constant pressure. Type 1 of Fig. 11. A large number of cycles. Material CS1026. Data after Hassan et al. (1992).

$\epsilon_{xc}$ = 0.5% and $\bar{\sigma}_\theta$ = 0.178, and a high number of cycles ($N$ = 69). In all three cases, the model predicts the experimental data with very good accuracy. Finally, Fig. 15 presents the simulated strain-path $\epsilon_x - \epsilon_\theta$ with $\epsilon_{xc}$ = 0.5% and $\bar{\sigma}_\theta$ = 0.245 and the comparison against the corresponding experiment. It can be concluded that the model predictions are quite successful.

Two of the more advanced loading histories, namely the inclined path with positive slope (Type 2 in Fig. 11) and bowtie path (Type 4 in Fig. 11), were also simulated and compared with the experimental data in Corona et al. (1996). In both simulations, $\epsilon_{xc} = 0.5\%$, $\bar{\sigma}_{\theta a} = 0.06$ and $\bar{\sigma}_{\theta m}$ = 0.24. The experimental data and the simulation results versus the number of cycles $N$, are plotted in Fig. 16. An excellent fit of the numerical simulations with the experimental data was achieved. In addition, for those two loading histories, the simulated strain-paths and the corresponding experimental data are plotted in Fig. 17 (Type 2) and Fig. 19 (Type 4), while the simulated stress-paths and corresponding experimental data are plotted in Fig. 18 (Type 2) and Fig. 20 (Type 4). The model reproduces stress and strain paths with high accuracy.

Finally, a set of simulations and their comparison with the experimental data for the case of axial cyclic stress-symmetric loading with constant internal pressure are presented in Fig. 21. Those tests induce double ratcheting, i.e., the plastic strain accumulates in both the axial and circumferential directions, simultaneously. This is possibly the most difficult loading to simulate. The proposed model shows qualitative and partially not quantitative accuracy in this case.

To clarify the source of this quantitative inaccuracy, it is first emphasized that the CS1026 specimens tested in Hassan et al. (1992), and simulated in this work, are cyclically stabilized. Thus, any tendency for cyclic hardening/softening does not appear due to the method of material treatment, but it might be related to the characteristics of this MR case. Moreover, Fig. 21 emphasizes the role of the increasing magnitude of the applied internal pressure, and thus, the role of the increasing magnitude of $\sigma_\theta$ on the rates of ratcheting in both the axial and circumferential directions. In Fig. 21, when $\sigma_\theta$ increased from 0 (red open circles) to 0.353 (black open circles), a decrease in both the accumulated positive axial and negative circumferential strain components was observed first (e.g., case of $\sigma_\theta$ = 0.210), while further $\sigma_\theta$ increase led to an increased ratcheting rate in both axial and circumferential directions ratcheting and an increased rate of circumferential ratcheting, evident in the case of $\sigma_\theta$ = 0.353 when compared against the case of $\sigma_\theta$ = 0.210. This complex effect on the two ratcheting mechanisms is thoroughly discussed in Hassan et al. (1992) and is simulated with qualitative accuracy and partial quantitative accuracy

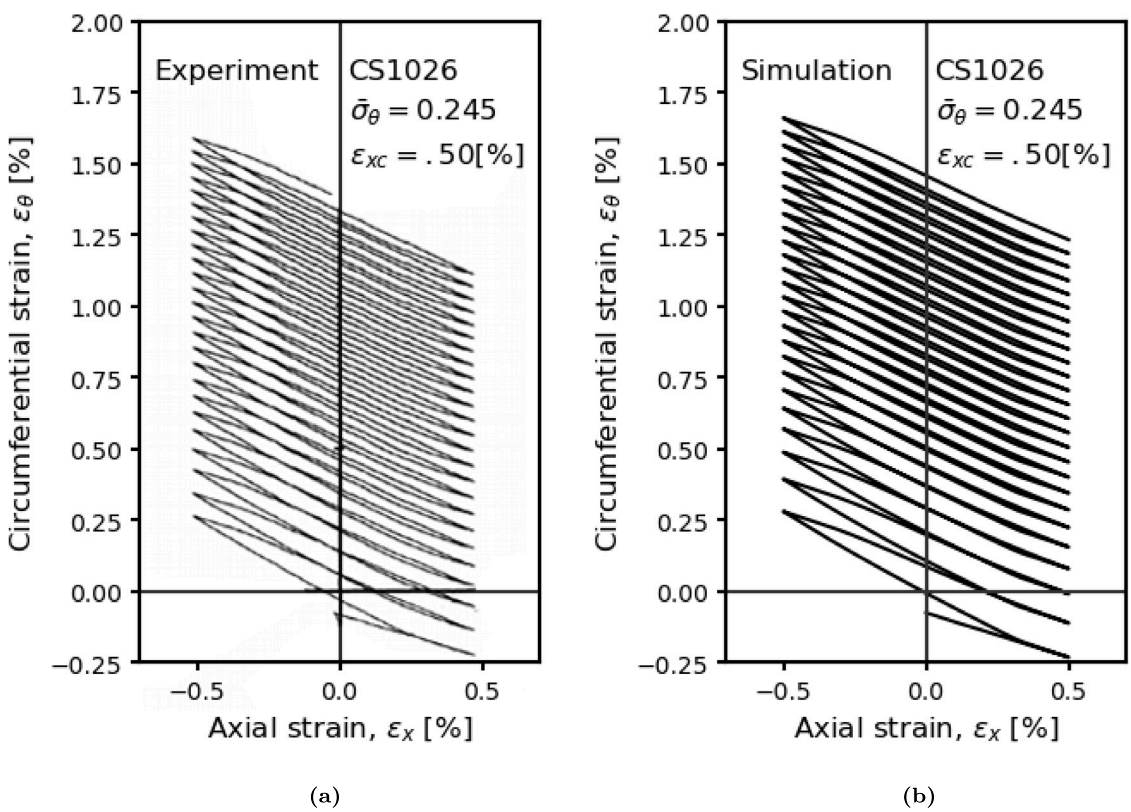


**Fig. 15.** Strain-path for axial strain-symmetric cycling at constant pressure. Type 1 of Fig. 11. Material CS1026. (a) Experiment after Hassan et al. (1992); (b) Simulation.

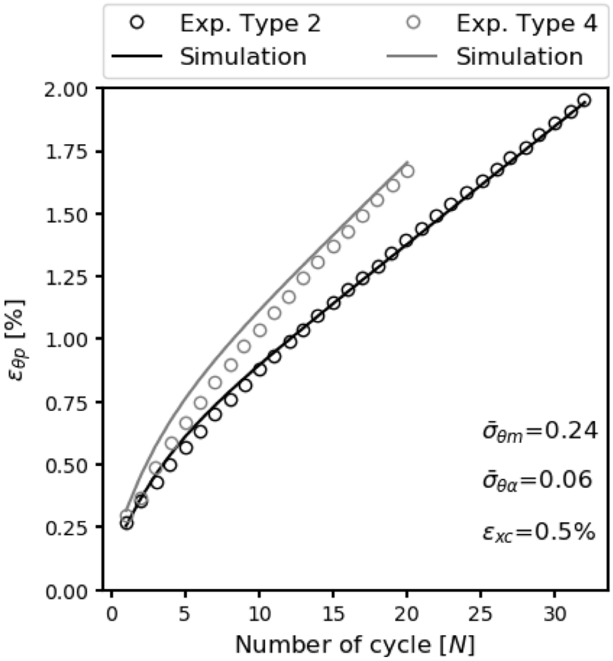


**Fig. 16.** Inclined path, positive slope, Type 2 in Fig. 11, and bowtie, Type 4 in Fig. 11, multiaxial ratcheting data and simulations. Material CS1026. Data after Corona et al. (1996).

by our model as can be seen in Fig. 21, which shows a significant improvement if compared to Fig. 19 of the aforementioned reference. We want to emphasize that this improvement is mainly related to the fact that our model simulated accurately the direction of ratcheting, as shown for all the cases in Fig. 21 by the accurate slopes of the graphs, with only the exception of the slope for $\bar{\sigma}_\theta = 0.249$. This accurate slope simulation is mainly due to the varying flow rule of the model induced by the BCD modification parameter $r_a$ given by Eq. (21). However, our model fails to simulate accurately the magnitude of the accumulated ratcheting in both directions for most of the cases, reflected in the length of the graphs, hence, we characterized the simulations as partially quantitatively accurate.

To further highlight the source of this inaccuracy, the simulated axial stress–strain and axial–circumferential strain relationships and their comparison against the experimental data in the case of $\sigma_\theta = 0.353$ are plotted in Fig. 22. It is concluded that the model overestimates the ratcheting rates in both directions (Figs. 22(c) and 22(d)) by about the same factor, hence the success in simulating the slope in Fig. 21, since it does not predict the instant “hardening” in the axial stress–strain relationship observed in the experiment (Fig. 22(a)) that leads to a decrease in the rate of ratcheting in the circumferential direction also (Fig. 22(b)). A more detailed investigation of this response is needed, and it will be included in future research work. Overall, though, the model performs better than the original Dafalias/Popov BS model and other state-of-the-art constitutive models in the literature (Welling et al., 2017; Hassan et al., 1992). Future

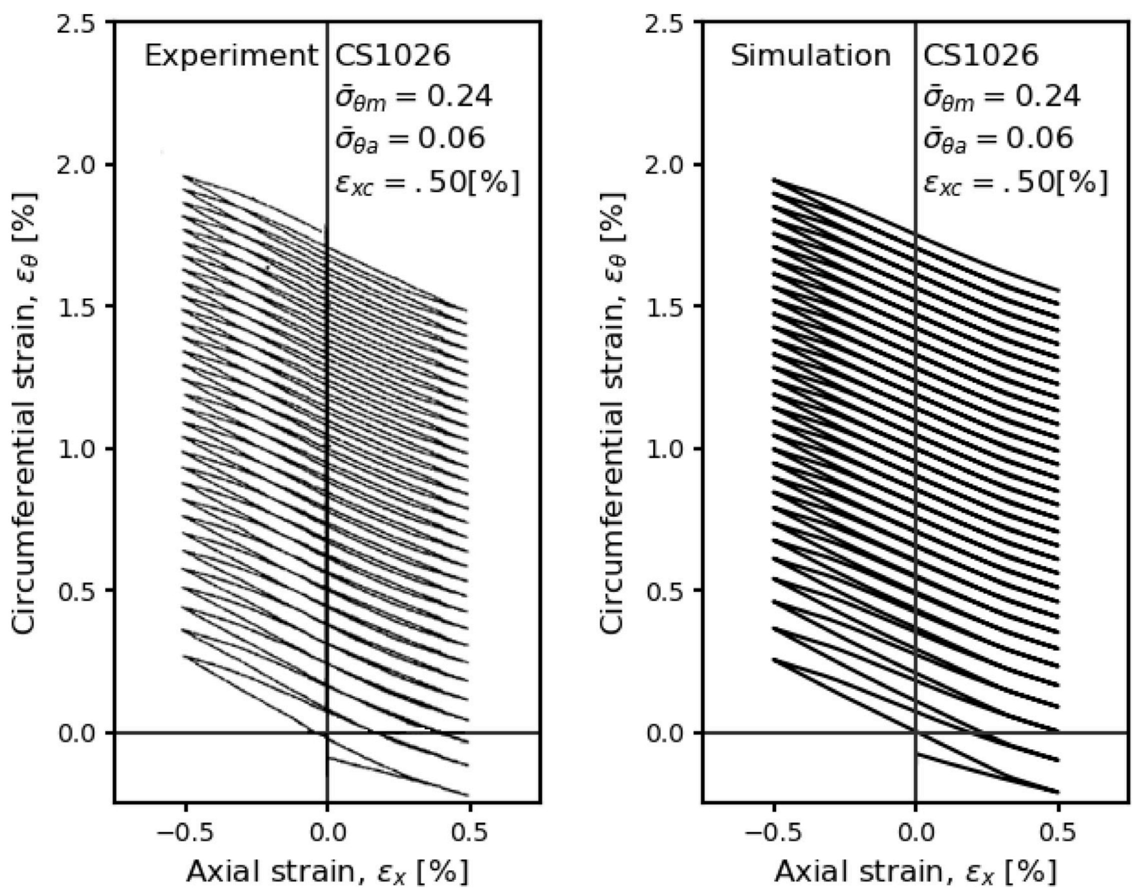


(a) (b)

**Fig. 17.** Strain-path for an inclined path with positive slope. Type 2 in Fig. 11. Material CS1026. (a) Experiment after Corona et al. (1996); (b) Simulation.

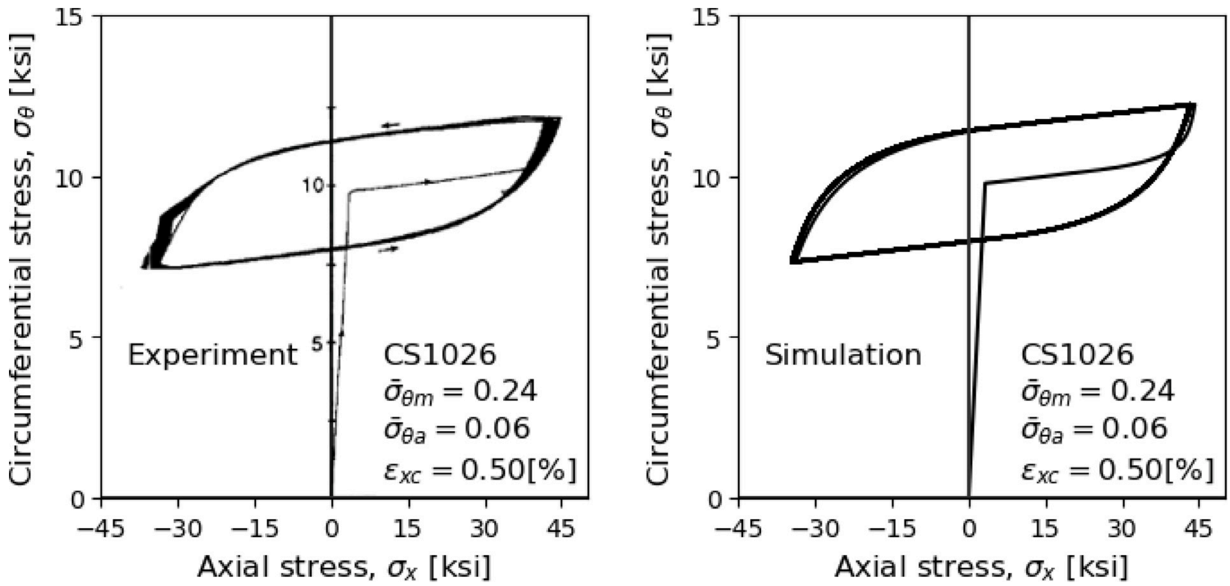


(a) (b)

**Fig. 18.** Stress-path for an inclined path with positive slope. Type 2 in Fig. 11. Material CS1026 (a) Experiment after Corona et al. (1996); (b) Simulation.

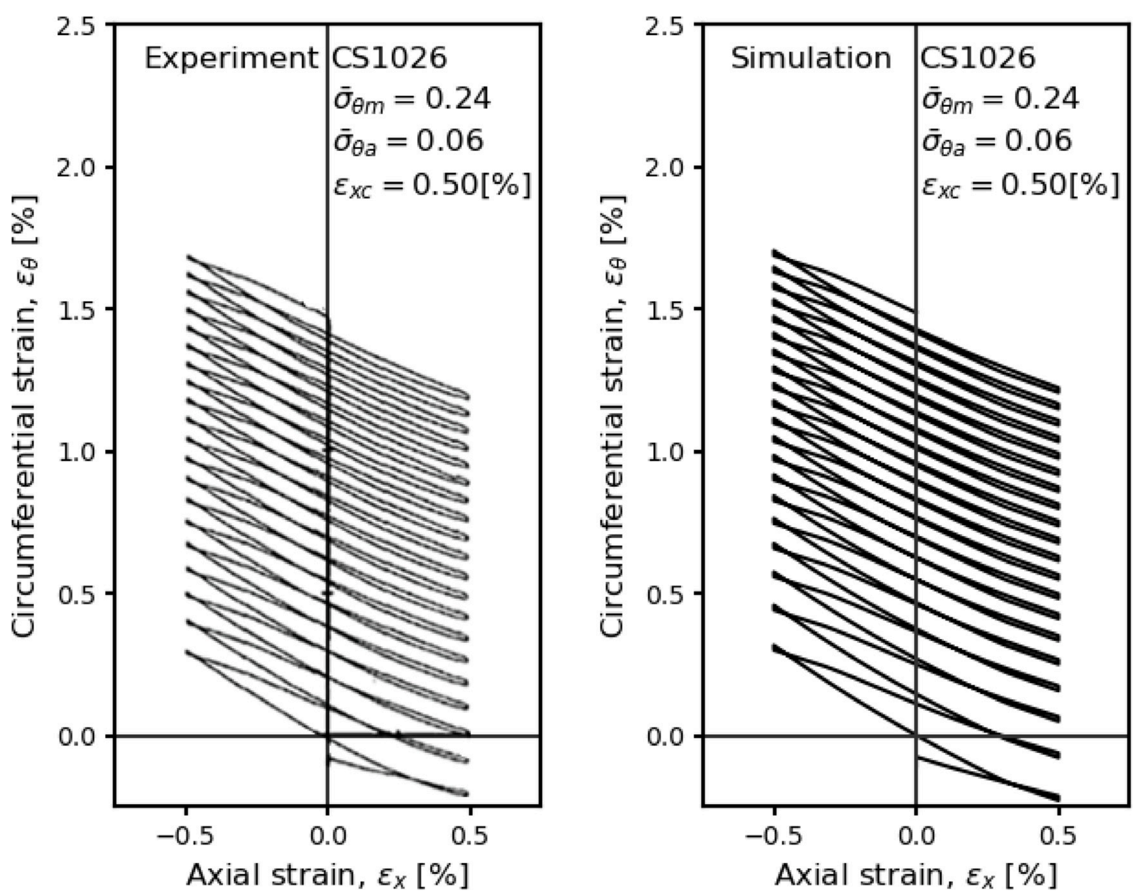


(a) (b)

**Fig. 19.** Strain-path, bowtie. Type 4 in Fig. 11. Material CS1026. (a) Experiment after Corona et al. (1996); (b) Simulation.

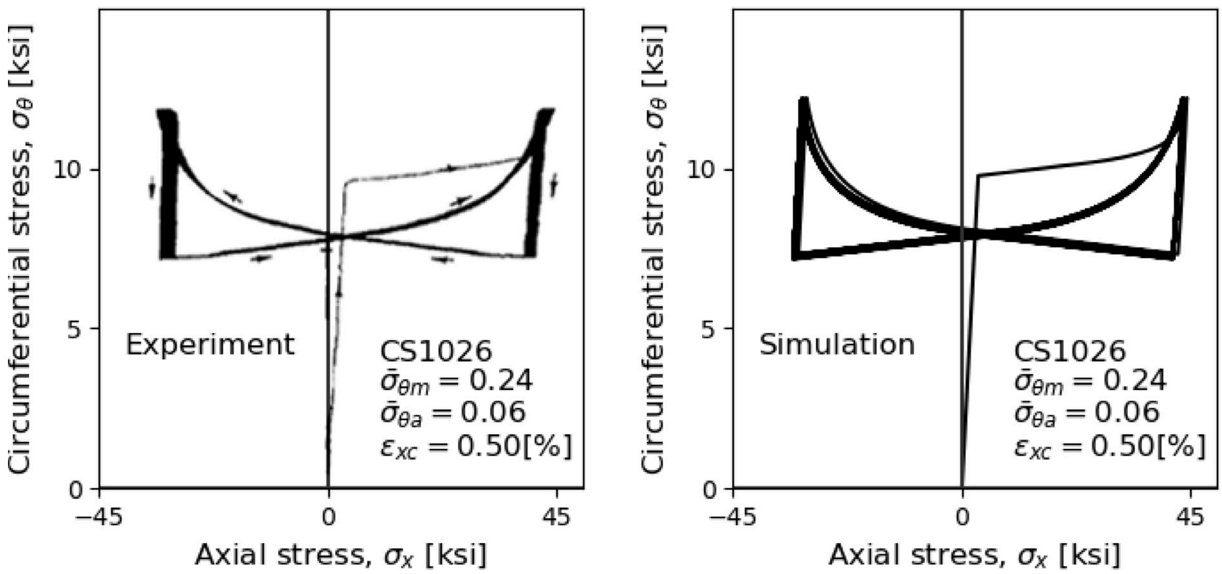


(a) (b)

**Fig. 20.** Stress-path, bowtie (Type 4 in Fig. 11). (a) Experiment after Corona et al. (1996); (b) Simulation. Material CS1026.

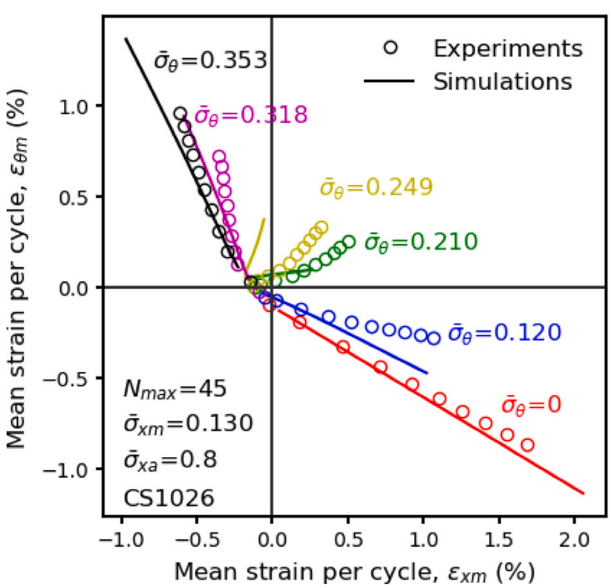


**Fig. 21.** Mean axial versus mean circumferential strain recorded at each cycle in stress-controlled axial cycling experiments at different values of $\bar{\sigma}_\theta$. Each data point (open circles) equals the values at every fifth cycle. Data after Hassan et al. (1992).

research is needed to accurately predict the material behavior under this loading condition.

### 5.3. Material CS1018

Three MR experiments, namely the inclined path, negative slope (3), the reverse bowtie path (5), and hourglass (6) shown in Fig. 11, are simulated for CS1018 specimens. Similarly, to the previous cases, the stabilization cycling of the specimens is not simulated, however, the choice of model parameters reflects the stabilized state of the material, and the initial point is adjusted to match the experimental findings. The results are presented in Fig. 23. A very good agreement of the simulation results with the experimental data is observed when plotted against the number of cycles $N$. In addition, the simulated strain paths of those three loading conditions are presented in Fig. 24 (hourglass (6), 17 cycles), Fig. 26 (inclined path, negative slope (3), 40 cycles) and Fig. 28 (reverse bowtie (5), 20 cycles). Similarly, the simulated stress-paths are presented in Fig. 25 (hourglass (6)), Fig. 27 (inclined path, negative slope (3)), and Fig. 29 (reverse bowtie (5)). The corresponding experimental data from Corona et al. (1996) are juxtaposed to the simulations of Figs. 24–29 for comparison. The conclusion is that model can predict very accurately these observed stress and strain paths.

## 6. Conclusion

The new SANIMETAL-BCD Bounding Surface (BS) model is based on a simple modification of the existing SANISTEEL BS model (Mahan et al., 2011), without introducing additional complex constitutive features, such as memory surfaces in stress space or non-hardening regions in strain space proposed mainly in conjunction with MAF models. Still, it can provide equally good or better simulations than these other more complex constitutive models for UR and MR cases, without losing the simulative capabilities for the much simpler monotonic or symmetric cyclic loading. This is because all the endemic advantages of BS plasticity are still present in the new model, in particular, the following two:

1. The decoupling of the value of the plastic modulus from the direction of the KH of the YS, and
2. The option to choose any kind of KH for the BS that is deemed necessary for more accurate simulation, without changing the other constitutive features.

One then can identify the following novel constitutive ingredients of the SANIMETAL-BCD model, in order of appearance in the paper. First, the BS acts as a changing bounding locus in stress space for the back stress (center of the YS) rather than the stress itself; this is a feature already introduced in soil models (Manzari and Dafalias, 1997; Dafalias and Manzari, 2004; Taiebat and Dafalias, 2008), but it is the first time it was applied to metals.

Second, and most important, is the introduction of the BCD modification into the relative KH of the YS in regard to the KH of the BS, as eloquently portrayed by the key Eq. (15). So far, the BCD

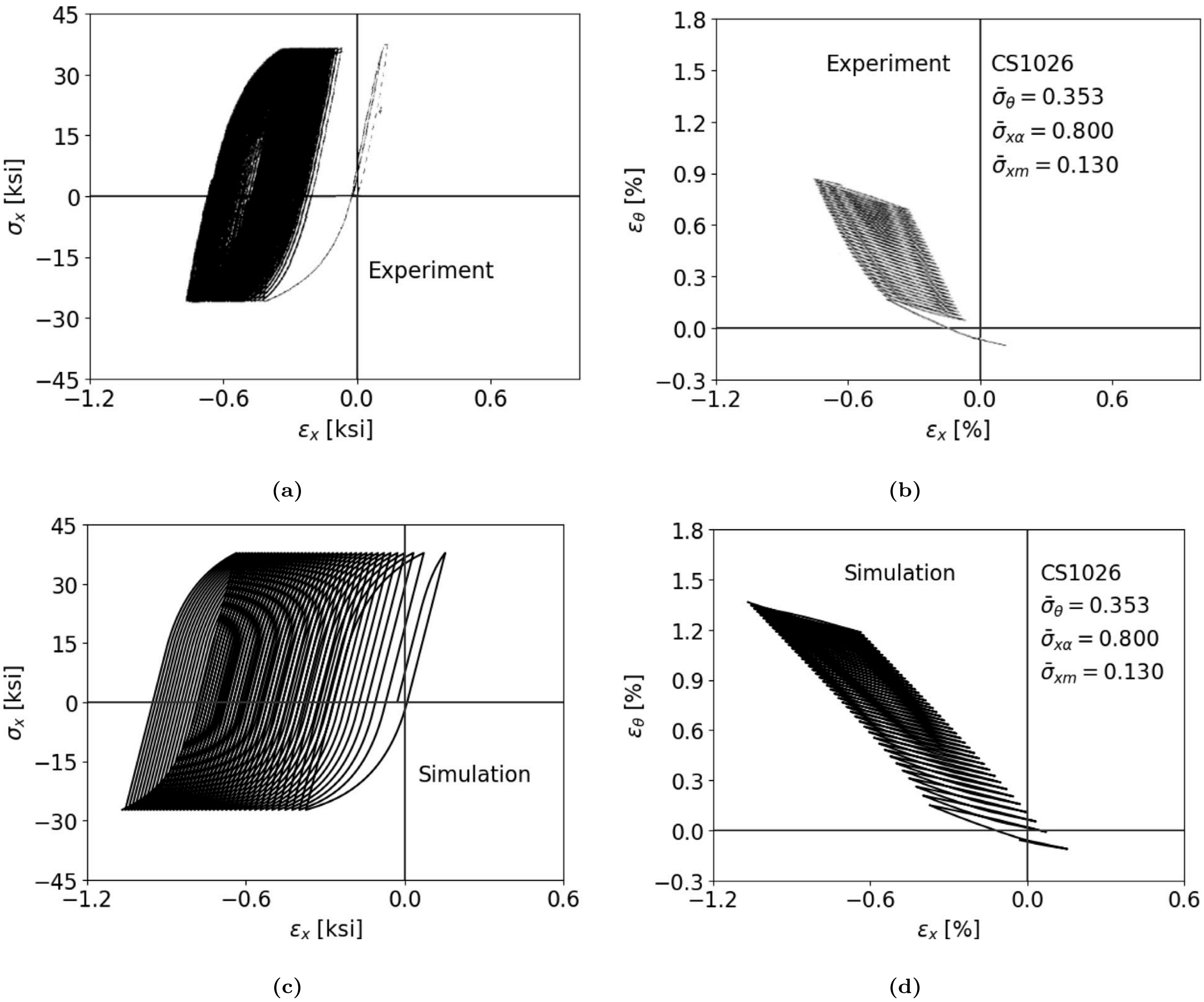


**Fig. 22.** Stress-controlled multiaxial axial cycling. Axial stress–strain experimental (a) and simulated (c) response. Axial–circumferential experimental (b) and simulated (d) response. Data after Hassan et al. (1992).

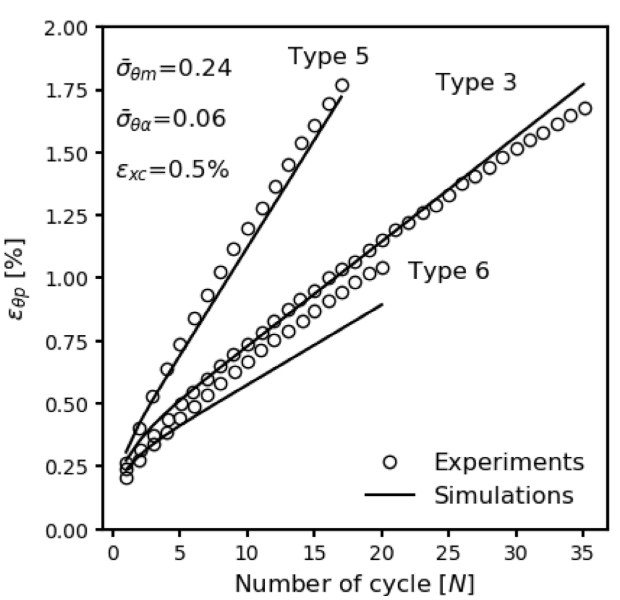


**Fig. 23.** Multiaxial ratcheting, reverse bowtie path (Type 5), inclined path, negative slope (Type 3), and hourglass (Type 6). Data after Corona et al. (1996). Material CS1018.

modification was applied to AF type of models, in which case there is no notion of relative KH. This modification was the key to controlling the direction of the plastic strain rate tensor (associative flow rule) during the loading process, hence, it is the basis for the successful simulation of MR.

The third novel ingredient, closely related to the second and motivated by a prior suggestion of Dafalias and Feigenbaum (2011) within the setting of MAF models, was the substitution of the variable $r_\alpha$ for the fixed-value modification parameter $\delta$ in the classical BCD modification of AF and MAF models. The $r_\alpha$ was expressed in Eq. (21) as a function of $r$, defined in Eq. (20) and measuring the proximity of the back stress to its BS. Despite its simplicity, Eq. (21) plays a role of cardinal importance for the effectiveness of the introduced BCD modification in regard to the successful simulations of MR for complex cyclic loading shown in previous figures for many cases. This has been confirmed by attempting the same simulations with a fixed value of $r_\alpha$, as is the case of fixed-value modification parameter $\delta$, which yielded significantly inferior simulations. In addition, the use of $r_\alpha$ easily satisfies the requirement $r_\alpha > 0.5$ at $r = 1$ on the BS, for avoiding crossing of the BS by the back stress of the YS under some loading conditions that can induce unjustified softening, a shortcoming of several MAF models which use $\delta < 0.5$ (Dafalias and Feigenbaum, 2011).

The fourth novel constitutive ingredient is the use of the special Dafalias/Ranzbari (DR) KH (see Mahan et al., 2011) for the BS, which

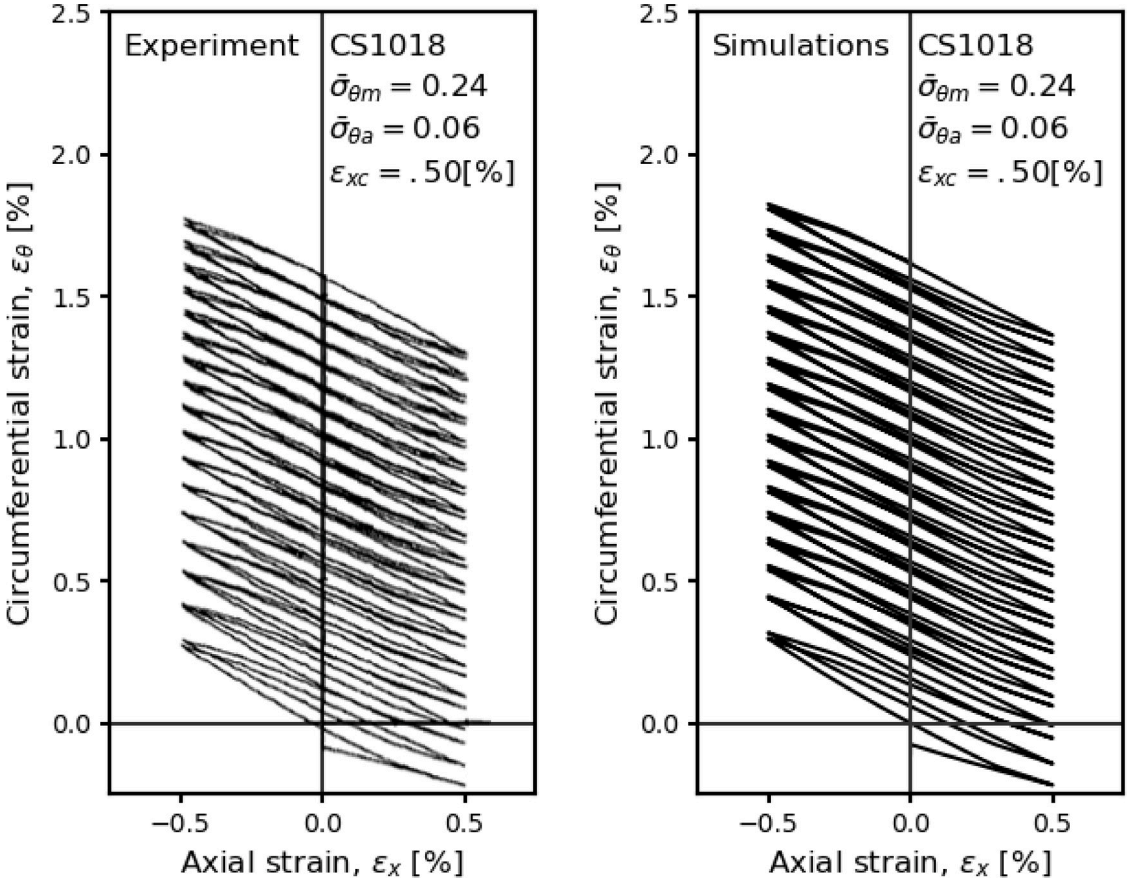


(a) (b)

**Fig. 24.** Strain-path, hourglass (Type 6 in Fig. 11). (a) Experiment after Corona et al. (1996); (b) Simulation. Material CS1018.

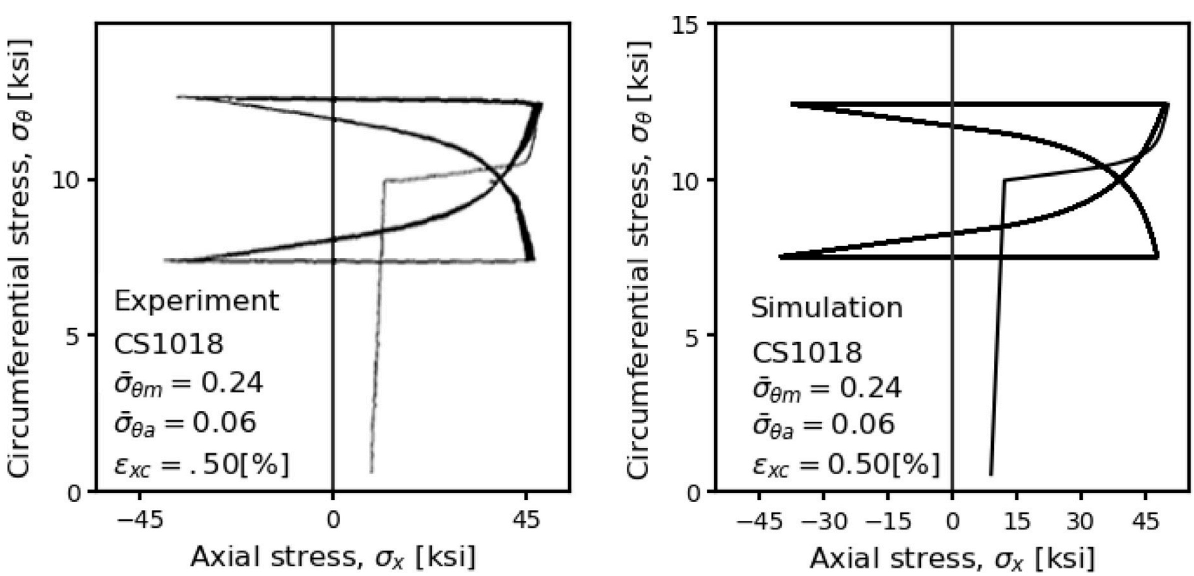


(a) (b)

**Fig. 25.** Stress-path, hourglass (Type 6 in Fig. 11). (a) Experiment after Corona et al. (1996); (b) Simulation. Material CS1018.

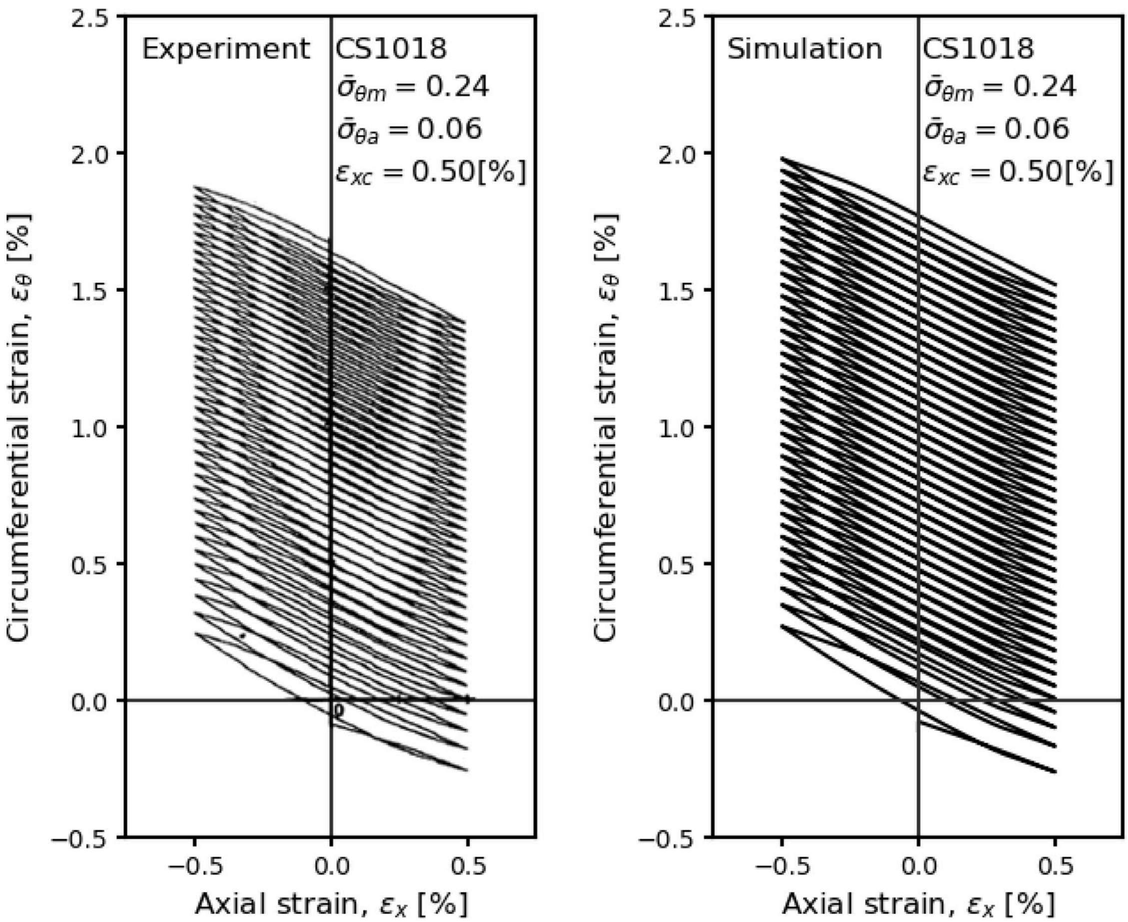


(a) (b)

**Fig. 26.** Strain-path for an inclined path with a negative slope (Type 3 in Fig. 11). (a) Experiment after Corona et al. (1996); (b) Simulation. Material CS1018.

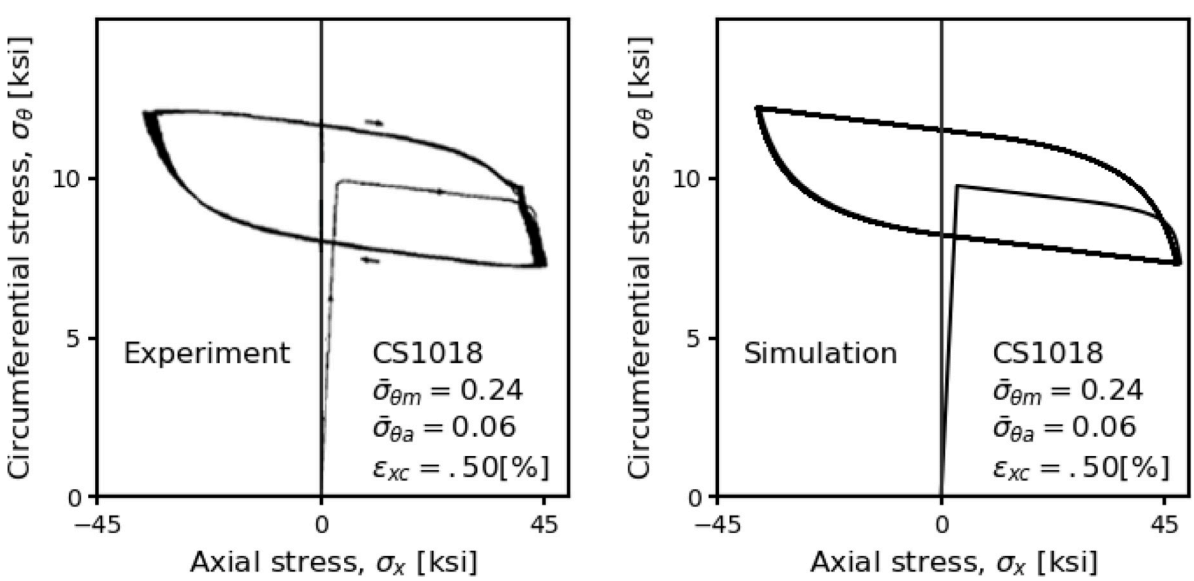


(a) (b)

**Fig. 27.** Stress-path for an inclined path with a negative slope (Type 3 in Fig. 11). (a) Experiment after Corona et al. (1996); (b) Simulation. Material CS1018.

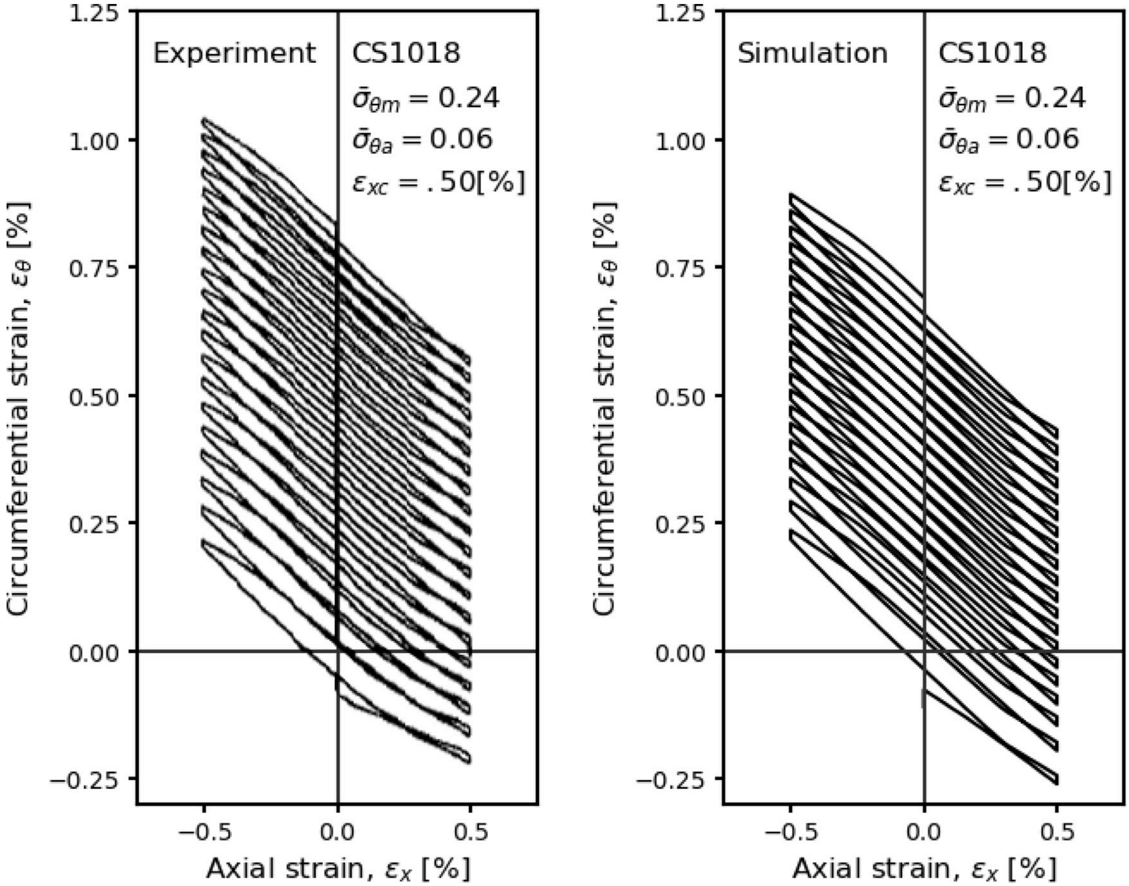


(a) (b)

**Fig. 28.** Strain-path for a reverse bowtie path (Type 5 in Fig. 11). (a) Experiment after Corona et al. (1996); (b) Simulation. Material CS1018.

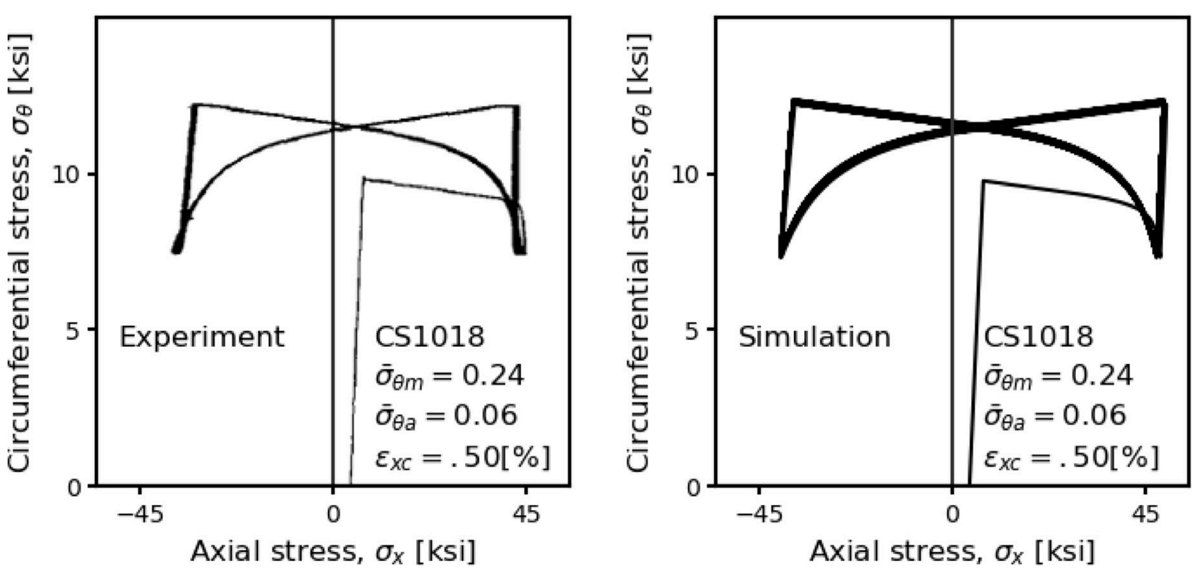


(a) (b)

**Fig. 29.** Stress-path for a reverse bowtie path (Type 5 in Fig. 11). (a) Experiment after Corona et al. (1996); (b) Simulation. Material CS1018.

induces a parallel "translation" of the bounds in uniaxial case towards the direction of ratcheting to maintain the continuation of UR, as observed in experiments. As already mentioned in the Introduction, this was a discovery made by Hassan and Kyriakides (1992, 1994a), but in these references the DR KH for the BS was used only for obtaining the ensuing bounding plastic modulus, while the KH direction of the YS was defined by an independent AF KH, followed by the KH for the BS via its interaction with it. In the present work, the approach is simpler and more straightforward: the DR KH was used directly for the BS for obtaining both the important bounding plastic modulus by the consistency condition for the BS, and the direction of KH for the BS, entering Eq. (15) for the relative KH of YS and BS, without the need to specify an independent AF type of KH for the YS. The flexibility of such YS KH was delegated instead to the use of the aforementioned third novel ingredient, namely the BCD variable modification parameter $r_\alpha$. A word of caution is that the DR KH for prolonged monotonic loading behaves like a linear KH, and its unrealistic effect when no reverse loading takes place must be appropriately modified if the need for such prolonged monotonic loading ever arises.

The results show that, in general, the model's simulations agree quite satisfactorily with experimental findings under a wide array of UR and MR loading conditions for all three kinds of carbon steel examined in this work. The lower accuracy of the model in the case of multiaxial cyclic stress-symmetric loading with constant internal pressure, which induces double ratcheting of plastic strain in the axial and circumferential directions simultaneously, was highlighted in this work and is a shortcoming characterizing all other available state-of-the-art models at present. More research is needed to improve its performance in this most complex case.

Another issue not addressed yet with the present model, is the possible effect of non-proportionality under multiaxial loading on the IH (Hassan and Kyriakides, 1994b); one of the reasons it was not addressed here is that materials used were cyclically stabilized before being subjected to UR and MR loading paths and after this stabilization, no additional IH is expected. The IH can include also isotropic softening under cyclic loading, and that can be another objective to be investigated in subsequent research. Finally, it will be important to address non-proportional loading that involves also a change of stress principal axes (non-coaxiality), as it happens when shear stress is cyclically applied; the non-proportional (non-radial) cases presented here, maintained the same stress principal axes directions. A prominent tool for such cases may be the novel formulation of split stress rate plasticity by Dafalias (2022), which differentiates the effect of a stress rate part causing change of stress principal stress axes, only, from the stress rate part causing change of stress principal values, only.

## Declaration of competing interest

The authors declare that they have no known competing financial interests or personal relationships that could have appeared to influence the work reported in this paper.

## Data availability

Data will be made available on request

## Acknowledgments

Support by the US Army Research Laboratory and US Army Research Office under Grant no. W911NF-19-1-0040 to Northern Arizona University and the University of California, Davis, by the Ministry of Education, Youth and Sports of the Czech Republic (Centre of Excellence for Nonlinear Dynamic Behavior of Advanced Materials in Engineering—CeNDYNMAT, grant number CZ.02.1.01/0.0/0.0/15_003/0000493; INTER-ACTION, LTA USA 18199), by the Czech Science Foundation (grant number 23-05338S), and by the Institute of Thermomechanics of the Czech Academy of Sciences (grant number RVO:61388998), is gratefully acknowledged. The authors would also like to acknowledge Despoina Papadopoulou for her help with the creation of high-quality figures for this work.

## Appendix

In a formulation where the BS refers to the stress rather than the back-stress (the original formulation), the $c$ was given as Mahan et al. (2011):

$$c = \frac{h_0}{\sqrt{3/2}\langle(\boldsymbol{\delta}_{in} - \boldsymbol{\delta}) : \boldsymbol{n}\rangle} \tag{A.1}$$

instead of Eq. (17), with $h_0$ a parameter, tensor $\boldsymbol{\delta} = \bar{\boldsymbol{s}} - \boldsymbol{s}$ representing the "distance" of current stress $\boldsymbol{s}$ from its image bounding stress $\bar{\boldsymbol{s}}$, and the subscript "in" implying its value at the initiation of a loading process. The $c$ of Eq. (A.1) was multiplied by $\boldsymbol{\delta} : \boldsymbol{n} = (\bar{\boldsymbol{s}} - \boldsymbol{s}) : \boldsymbol{n}$ in Mahan et al. (2011). Based on Eq. (13) one can derive that $\boldsymbol{\delta} = \bar{\boldsymbol{s}} - \boldsymbol{s} = \boldsymbol{\alpha}^b - \boldsymbol{\alpha}$ and similarly for the initial values $\boldsymbol{\delta}_{in} = \bar{\boldsymbol{s}}_{in} - \boldsymbol{s} = \boldsymbol{\alpha}^b_{in} - \boldsymbol{\alpha}_{in}$ (the latter relation was already used in what follows Eq. (18)). Therefore, firstly one has $\boldsymbol{\delta} : \boldsymbol{n} = (\bar{\boldsymbol{s}} - \boldsymbol{s}) : \boldsymbol{n} = \left(\boldsymbol{\alpha}^b - \boldsymbol{\alpha}\right) : \boldsymbol{n}$, hence, the same quantity multiplies the $c$ of Eq. (A.1) in Mahan et al. (2011), and the $c$ of Eq. (17) when it appears in Eq. (16) for the plastic modulus $K^p$. However, this is not the case with the denominators of Eqs. (17) and (A.1) that determine the corresponding $c$ in each case. Based on the foregoing one can write:

$$\begin{aligned}\left(\boldsymbol{\delta}_{in} - \boldsymbol{\delta}\right) : \boldsymbol{n} &= \left[\left(\boldsymbol{\alpha}^b_{in} - \boldsymbol{\alpha}_{in}\right) - \left(\boldsymbol{\alpha}^b - \boldsymbol{\alpha}\right)\right] : \boldsymbol{n} \\ &= \left[(\boldsymbol{\alpha} - \boldsymbol{\alpha}_{in}) - (\boldsymbol{\beta} - \boldsymbol{\beta}_{in}) + \sqrt{2/3}\left[(K_{in} - K) - (k_{in} - k)\right]\boldsymbol{n}\right] : \boldsymbol{n}\end{aligned} \tag{A.2}$$

where use of Eq. (13) was made in deriving the last member of Eq. (A.2). It follows from Eq. (A.2) that the denominators of Eqs. (17) and (A.1) are not the same. If one assumes that the change of the values of $K$ and $k$ due to IH is not large and their current values are close to their initial values, and simultaneously the change of the BS back stress $\boldsymbol{\beta}$ is small, hence $\boldsymbol{\beta} \approx \boldsymbol{\beta}_{in}$, it then follows that $\left(\boldsymbol{\delta}_{in} - \boldsymbol{\delta}\right) : \boldsymbol{n} \approx \left(\boldsymbol{\alpha} - \boldsymbol{\alpha}_{in}\right) : \boldsymbol{n}$ and the $c$'s of Eqs. (17) and (A.1) are approximately equal. The foregoing approximation assumptions on IH and $\boldsymbol{\beta}$, are not far from reality in practical terms.

## References

Armstrong, P.J., Frederick, C.O., 1966. A Mathematical Representation of the Multiaxial Baushinger Effect. Technical Report RD/B/N 731, General Electric General Board.

Bari, S., Hassan, T., 2001. Kinematic hardening rules in uncoupled modeling for multiaxial ratcheting simulation. Int. J. Plast. 17 (7), 885–905. http://dx.doi.org/10.1016/S0749-6419(00)00031-0.

Behravesh, S.B., Dafalias, Y.F., 2022. Two-surface cyclic plasticity. In: Jahed, H., Roostaei, A.A. (Eds.), Cyclic Plasticity of Metals. Modeling Fundamentals and Applications. Elsevier, pp. 101–138.

Burlet, H., Cailletaud, G., 1986. Numerical techniques for cyclic plasticity at variable temperature. Eng. Comput. 3 (2), 143–153. http://dx.doi.org/10.1108/eb023652.

Chaboche, J., Dang-Van, K., Cordier, G., 1979. Modelization of strain memory effect on the cyclic hardening of 316 stainless steel. In: Tansactions of the 5th International Conference on Structural Mechanics in Reactor Technology. Berlin, (Div L in 11/3).

Corona, E., Hassan, T., Kyriakides, S., 1996. On the performance of kinematic hardening rules in predicting a class of biaxial ratcheting histories. Int. J. Plast. 12 (1), 117–145. http://dx.doi.org/10.1016/S0749-6419(95)00047-X.

Dafalias, Y.F., 1975. On Cyclic and Anisotropic Plasticity (Ph.D. thesis). University of California at Berkeley.

Dafalias, Y.F., 1984. Modeling cyclic plasticity: Simplicity versus sophistication. In: Desai, C.S., Gallagher, R.H. (Eds.), Mechanics of Metarials. John Wiley and Sons, pp. 153–178.

Dafalias, Y.F., 1986. Bounding surface plasticity. i: mathematical foundation and hypoplasticity. J. Eng. Mech. 112 (9), 966–987.

Dafalias, Y.F., 2022. Split stress rate plasticity formulation. Int. J. Solids Struct. 257 (December 2021), 111494. http://dx.doi.org/10.1016/j.ijsolstr.2022.111494.

Dafalias, Y.F., Feigenbaum, H.P., 2011. Biaxial ratchetting with novel variations of kinematic hardening. Int. J. Plast. 27 (4), 479–491. http://dx.doi.org/10.1016/j.ijplas.2010.06.002.

Dafalias, Y.F., Kourousis, K.I., Saridis, G.J., 2008. Multiplicative AF kinematic hardening in plasticity. Int. J. Solids Struct. 45 (10), 2861–2880. http://dx.doi.org/10.1016/j.ijsolstr.2008.01.001.

Dafalias, Y.F., Manzari, M.T., 2004. Simple plasticity sand model accounting for fabric change effects. J. Eng. Mech. 130 (6), 622–634. http://dx.doi.org/10.1061/(ASCE)0733-9399(2004)130:6(622).

Dafalias, Y.F., Popov, E.P., 1974. A model of nonlinearly hardening materials for complex loading. In: 7th US National Congress of Theoretical and Applied Mechanics. Boulder, CO.

Dafalias, Y.F., Popov, E.P., 1975. A model of nonlinearly hardening materials for complex loading. Acta Mech. 21, 173–192.

Dafalias, Y.F., Popov, E.P., 1976. Plastic internal variables formalism of cyclic plasticity. J. Appl. Mech. 43, 641–646. http://dx.doi.org/10.1016/0093-6413(76)90079-3.

Delobelle, P., 1993. Synthesis of the elastoviscoplastic behavior and modelization of an austenitic stainless steel over a large temperature range, under uniaxial and biaxial loadings, part II: Phenomenological modelization. Int. J. Plast. 9 (1), 87–118. http://dx.doi.org/10.1016/0749-6419(93)90015-I.

Delobelle, P., Robinet, P., Bocher, L., 1995. Experimental study and phenomenological modelization of ratchet under uniaxial and biaxial loading on an austenitic stainless steel. Int. J. Plast. 11 (4), 295–330. http://dx.doi.org/10.1016/S0749-6419(95)00001-1.

Hassan, T., Corona, E., Kyriakides, S., 1992. Ratcheting in cyclic plasticity, part II: Multiaxial behavior. Int. J. Plast. 8 (2), 117–146. http://dx.doi.org/10.1016/0749-6419(92)90010-A.

Hassan, T., Kyriakides, S., 1992. Ratcheting in cyclic plasticity, part I: Uniaxial behavior. Int. J. Plast. 8 (1), 91–116. http://dx.doi.org/10.1016/0749-6419(92)90040-J.

Hassan, T., Kyriakides, S., 1994a. Ratcheting of cyclically hardening and softening materials: I. Uniaxial behavior. Int. J. Plast. 10 (2), 149–184. http://dx.doi.org/10.1016/0749-6419(94)90034-5.

Hassan, T., Kyriakides, S., 1994b. Ratcheting of cyclically hardening and softening materials: II. Multiaxial behavior. Int. J. Plast. 10 (2), 185–212. http://dx.doi.org/10.4337/9781849805896.00015.

Ishlinskii, A., 1954. General theory of plasticity with linear strengthening. Ukr. Mat. Zh. 6 (3), 314–324.

Krieg, R.D., 1975. A practical two surface plasticity theory. J. Appl. Mech. 42 (3), 641. http://dx.doi.org/10.1115/1.3423656.

Mahan, M., Dafalias, Y.F., Taiebat, M., Heo, Y., Kunnath, S., 2011. SANISTEEL : Simple anisotropic steel plasticity model. J. Struct. Eng. (February), 185–194.

Manzari, M.T., Dafalias, Y.F., 1997. A critical state two-surface plasticity model for sands. Géotechnique 47 (2), 255–272.

Marquis, D., 1979. Modelisation et Identification de l' Ecrouissage Anisotrope des Metaux (Ph.D. thesis).

Mróz, Z., 1967. On the description of anisotropic workhardening. J. Mech. Phys. Solids 15 (3), 163–175. http://dx.doi.org/10.1016/0022-5096(67)90030-0.

Prager, W., 1956. A new method of analyzing stresses and strains in work-hardening plastic solids. ASME J. Appl. Mech.1 23, 493–496.

Sayed-Ranjbari, M., 1986. Further development, multiaxial formulation and implementation of the bounding surface plasticity model for metals (Ph.D. thesis). University of California at Davis.

Taiebat, M., Dafalias, Y.F., 2008. SANISAND : Simple anisotropic sand plasticity model. Int. J. Numer. Anal. Methods Geomech. (32), 915–948. http://dx.doi.org/10.1002/nag.

Welling, C.A., Marek, R., Feigenbaum, H.P., Dafalias, Y.F., Plesek, J., Hruby, Z., Parma, S., 2017. Numerical convergence in simulations of multiaxial ratcheting with directional distortional hardening. Int. J. Solids Struct. 126–127, 105–121. http://dx.doi.org/10.1016/j.ijsolstr.2017.07.032.